54p.

N62-16810 21

NASA TN D-1399

NASA TN D-1399

TECHNICAL NOTE

D-1399

EFFECT OF AFTERBODY-EJECTOR CONFIGURATIONS ON THE PERFORMANCE AT TRANSONIC SPEEDS OF A PYLON-SUPPORTED NACELLE MODEL HAVING A HOT-JET EXHAUST

By John M. Swihart, Charles E. Mercer,
and Harry T. Norton, Jr.

Langley Research Center
Langley Station, Hampton, Va.

NATIONAL AERONAUTICS AND SPACE ADMINISTRATION

WASHINGTON October 1962

N62-16810

NATIONAL AERONAUTICS AND SPACE ADMINISTRATION

TECHNICAL NOTE D-1399

EFFECT OF AFTERBODY-EJECTOR CONFIGURATIONS ON THE PERFORMANCE AT TRANSONIC SPEEDS OF A PYLON-SUPPORTED NACELLE MODEL HAVING A HOT-JET EXHAUST[1]

By John M. Swihart, Charles E. Mercer,
and Harry T. Norton, Jr.

SUMMARY

An investigation of several afterbody-ejector configurations on a pylon-supported nacelle model has been completed in the Langley 16-foot transonic tunnel at Mach numbers from 0.80 to 1.05. The propulsive performance of two nacelle afterbodies with low boattailing and long ejector spacing was compared with that of a configuration corresponding to a turbojet-engine installation having a highly boattailed afterbody with a short ejector. The jet exhaust was simulated with a hydrogen peroxide turbojet simulator. The angle of attack was maintained at 0°, and the average Reynolds number based on body length was 20×10^{6}.

The results of the investigation indicated that the configuration with a conical afterbody with smooth transition to a 15° boattail angle had large beneficial jet effects on afterbody pressure-drag coefficient and had the best thrust-minus-drag performance of the afterbody-ejector configurations investigated.

INTRODUCTION

If the subsonic-cruise—supersonic-dash airplane is to perform efficiently at each speed condition, the primary nozzle, the ejector nozzle, and afterbody shape must be varied. The afterbody and ejector nozzle shape is usually varied with a double-flap arrangement at the turbojet-engine exit. During cruise flight with afterburner off, the nacelle has a much larger boattail angle than at supersonic flight with

[1]Supersedes declassified NASA MEMO 1-4-59L by John M. Swihart, Charles E. Mercer, and Harry T. Norton, Jr., 1959.

afterburner on. Several investigations have been conducted to evaluate the effect of boattailing on the performance of afterbodies (e.g., refs. 1 to 4) and to evaluate the internal performance of ejectors (refs. 5 to 9). The results of these investigations indicate that the performance of a typical pylon-supported nacelle installation with afterburner off (low spacing ratio and large boattail angle) could be improved if the ejector spacing ratio could be increased to allow a lower boattail angle.

An investigation was conducted in the Langley 16-foot transonic tunnel to evaluate the propulsive performance of afterbody-ejector combinations using a pylon-supported nacelle model with a hot-jet exhaust. Three afterbody shapes and two ejector configurations corresponding to nonafterburning arrangements were used in the investigation. The combined internal and external performance of a steeply boattailed body with a typical short ejector was compared with those for lower boattailed bodies with extended ejectors to determine if gains could be obtained with the compromise configurations. Tests were conducted at Mach numbers from 0.80 to 1.05 at an angle of attack of 0° and at primary jet total-pressure ratios from 1.0 (jet off) to 5.0. At each Mach number, the primary jet total-pressure ratio was varied over the range for several values of secondary air weight flow. A hydrogen peroxide turbojet simulator was used for the investigation. (See ref. 10.)

SYMBOLS

A	area, sq ft
C_D	drag coefficient, $\frac{D}{qA_{max}}$
C_d	flow coefficient, $\frac{w_p}{w_i}$
$C_{D,a}$	afterbody pressure-drag coefficient, $\sum \frac{C_p A_l}{A_{max}}$
$C_{D,ex}$	external-drag coefficient, $C_{D,a} + C_{D,fore}$
$C_{D,fore}$	forebody drag coefficient including model skin-friction-drag coefficient
C_F	thrust coefficient, $\frac{F}{qA_{max}}$

$C_{F,ej}$ ejector jet thrust coefficient, $\frac{F_{ej}}{qA_{max}}$

$C_{F_{i,c}}$ ideal jet thrust coefficient for convergent nozzle, $\frac{F_{i,c}}{qA_{max}}$

C_L lift coefficient, $\frac{L}{qA_{max}}$

C_m pitching-moment coefficient about 0.50 nacelle length, $\frac{\text{Pitching moment}}{qA_{max}X}$

C_p pressure coefficient, $\frac{p_l - p_\infty}{q}$

D drag, lb

d diameter, in.

F jet thrust, lb

F_{ej} ejector jet thrust,

$$F_p + m_s V_s + \int_{A_p}^{A_s} \left(p_l - p_\infty\right) dA + \int_{A_s}^{A_e} \left(p_l - p_\infty\right) dA, \text{ lb}$$

$F_{i,c}$ ideal jet thrust for convergent nozzle,

$$\frac{w_p}{g} \sqrt{\gamma g R \frac{2}{\gamma + 1} T_{t,j}} + A_p\left(p_p - p_\infty\right), \text{ lb}$$

F_p primary-nozzle jet thrust, lb

g gravitational acceleration, ft/sec^2

L distance from afterbody exit to nozzle exit, in.; lift, lb

l length of afterbody, in.

M free-stream Mach number

m mass flow, slugs/sec

p static pressure, lb/sq ft

p_t total pressure, lb/sq ft

$p_{t,j}/p_\infty$ ratio of primary jet total pressure to free-stream static pressure

q free-stream dynamic pressure, lb/sq ft

R gas constant, ft/°R

r model radius, in.

T_t stagnation temperature, °R

V velocity, ft/sec

w weight flow, lb/sec

w_i ideal weight flow for sonic exit,

$$p_{t,j}A_p\left(\frac{2}{\gamma + 1}\right)^{\frac{\gamma+1}{2(\gamma-1)}}\sqrt{\frac{\gamma g}{RT_{t,j}}}, \text{ lb/sec}$$

$\frac{w_s}{w_p}\sqrt{\frac{T_{t,s}}{T_{t,p}}}$ corrected secondary-to-primary weight-flow ratio

X total nominal length of model, 60 in.

x longitudinal distance from reference point, positive rearward, in.

γ ratio of specific heats

θ meridian angle, positive counterclockwise looking forward from afterbody exit, deg

Subscripts:

a afterbody

b base

bal balance

e exit of afterbody

ex	external
f	primary nozzle base
fore	forebody
j	jet
l	local
max	maximum
p	primary nozzle
s	seal, secondary
∞	free-stream conditions
1	forward compartment
2	outer compartment
3	secondary air passage
4	tailpipe

APPARATUS AND METHODS

Wind Tunnel

This investigation was conducted in the Langley 16-foot transonic tunnel, which is a single-return atmospheric wind tunnel with an octagonal slotted test section and continuous air exchange. It has a speed range from a Mach number of 0.20 to about 1.10 and the Mach number is varied by changing rotational speed of drive fans.

Tests

For this investigation the model was held at an angle of attack of 0° throughout the Mach number range from 0.80 to 1.05. The average Reynolds number based on body length was about 20×10^{6}. The hydrogen peroxide turbojet-engine simulator was operated at ratios of primary

jet total pressure to free-stream static pressure from 1.0 (jet off) to 5.0 at all Mach numbers. For the effect of secondary air on the net performance, a complete range of secondary air weight flow from 0 (no flow) to approximately 0.25 lb/sec was investigated; however, in this paper only the values of 0, 0.06, and 0.20 lb/sec of secondary air weight flow are presented.

An investigation was made to determine the interference effect of the pylon on model pressure distributions. A comparison was made of the pylon-supported model, a sting-mounted model, and the pylon-supported model with a dummy sting. For all these tests, the turbojet-engine simulator was off.

Model and Support System

A sketch of the pylon-supported nacelle turbojet-engine simulator model used in the investigation is presented in figure 1 and is described in reference 11. A photograph of the model installed in the test section of the Langley 16-foot transonic tunnel is given in figure 2. The nacelle consisted of an ogival forebody, a cylindrical centerbody having a maximum diameter of 6.50 inches, and afterbodies which were detachable at the 48.875-inch station.

The afterbodies consisted of three configurations which were designed for nonafterburner cruise flight at a Mach number of about 0.90. A sketch of the afterbodies giving dimensions, pressure-orifice locations, and relative position of the turbojet-engine simulator nozzle is presented in figure 3. Afterbody I, which was considered to be the basic afterbody tested, had a spacing ratio of 0.789 and a boattail angle of 28°. This afterbody was selected because it represented some current nacelle designs. Both afterbody II and afterbody III had a spacing ratio of 1.440 and a boattail angle of 15°. They were selected to give a lower afterbody drag and also to determine whether spacing ratio would cause a loss in ejector jet thrust. The only difference between afterbodies II and III was the generous radius of curvature applied to afterbody III at the start of the conical boattail. (See fig. 3.) A photograph showing the three afterbodies is presented in figure 4.

The support system consisted of a conventional sting with an integral sweptforward pylon on the forward end inverted with reference to a normal underwing mounting. The nacelle was attached to the pylon through a four-component internal strain-gage balance. A separate thrust measuring system was also mounted from the pylon support with a hydrogen peroxide turbojet-engine simulator connected to the thrust balance. A

schematic diagram showing the thrust and drag systems with the pressures and areas affected by each is shown in figure 5.

In order to evaluate the interference effect of pylon strut support on external drag, the nacelle was attached through the four-component internal balance to a conventional sting passing through the rear of the model. The sting consisted of a cylindrical section 2 inches in diameter with a conical half-angle of 5.0° which began at station 63.39. The pylon support system with a dummy sting of the same type described previously was also used to give a comparison of effect on afterbody drag. A photograph showing the different support systems with afterbody III installed in the tunnel test section is presented in figure 6.

Secondary air was used as a coolant for the turbojet-engine simulator and also to compare the effect of secondary air quantity on the ejector thrust characteristics. The secondary air came through the pylon support system and was distributed through small openings of 1/16-inch diameter around the turbojet-engine simulator. (See figs. 1 and 5.)

A hydrogen peroxide turbojet-engine simulator similar to that described in reference 10 was used for this investigation. The simulator unit produces a hot-jet exhaust ($1,820^{\circ}$ R) which is very similar to the exhaust of a turbojet engine.

Instrumentation

Pressures were measured at several meridian angles around the afterbody, on the inside of the afterbody (ejector wall), and on the outside of the primary-nozzle flap. (See fig. 3.) In addition, primary jet total pressures, secondary air inlet and exit static pressures, and primary and secondary total temperatures were measured. (See fig. 5.) For the basic tests the pressure tubing from each orifice was conducted out of the nacelle through the pylon support and connected to an electrical pressure transducer located in the sting barrel. The electrical pressure transducers were manifolded to a common reference pressure and the whole transducer manifold system was immersed in a constant-temperature bath to keep both the zero and sensitivity shifts of the transducers to a minimum. For the interference tests the pressures were measured with a multiple-tube mercury manometer.

Forces and moments on the nacelle were measured by a four-component strain-gage balance. The thrust forces of the simulator were measured on a one-component thrust balance. (See fig. 5.)

Primary jet weight flow was measured by using a vane-type electronic flowmeter located in the hydrogen peroxide supply line (ref. 10). A

standard venturi with a 1-inch-diameter throat located in the air supply line was used to measure the secondary flow passing through the model.

Data Reduction

Electrical signals from the pressure transducers were transmitted to carrier amplifiers and then to recording oscillographs located in the tunnel control room. The pressures, forces, and temperatures were converted to standard pressure and force coefficients by machine computation from the trace deflections on the paper film. It should be noted that positive normal force is down for this test setup, since the model is considered to be inverted from a normal underwing pylon mounting.

Drag system.- The drag component of the main balance measured the axial forces on the external surface of the nacelle and the force on the inside of the afterbody to the center of the rear seal of the model (see figs. 1 and 5), plus an internal pressure force. The equation for the external drag is as follows:

$$D_{ex} = D_{bal} + \left(p_l - p_\infty\right)A_{s,1} + \left(p_2 - p_\infty\right)\left(A_{s,2} - A_{s,1}\right) + \int_{A_{s,2}}^{A_e}\left(p_l - p_\infty\right)dA$$

Afterbody drag forces were obtained from the integrated pressures over the afterbody. The external drag of the nacelle assembly is defined as the sum of all the axial forces acting on the external surfaces of the model to the ejector exit, or simply the afterbody drag plus the forebody drag. Therefore, the forebody drag is as follows:

$$D_{fore} = D_{ex} - D_a$$

Figure 5 shows the location of the balance, areas, and pressures used in the external-drag equation. It is to be noted that the forebody drag includes the forebody pressure and viscous drag plus afterbody skin-friction drag. Figure 7 shows effect of Mach number on forebody drag coefficient and on the forebody drag coefficient with calculated afterbody skin-friction-drag coefficient removed. The afterbody skin-friction-drag coefficient was calculated for a turbulent boundary layer. These data are an average of all configurations tested and include pylon interference on the forebody drag.

Thrust system.- The thrust balance measured the primary nozzle thrust and some internal forces, plus the incoming momentum and pressure force of the secondary air. The primary nozzle thrust was obtained as follows:

$$F_p = F_{bal} - m_s V_{s,3} - \left(p_3 - p_\infty\right)\left(A_{s,2} - A_4\right) + \left(p_1 - p_\infty\right)\left(A_{s,2}\right) - \left(p_f - p_\infty\right)\left(A_4 - A_p\right)$$

where the location of the balance, areas, and pressures are presented in figure 5.

The ejector thrust is obtained in the following manner:

$$F_{ej} = F_p + m_s V_s + \int_{A_p}^{A_s} \left(p_l - p_\infty\right) dA + \int_{A_s}^{A_e} \left(p_l - p_\infty\right) dA$$

The propulsive force can now be obtained by taking the difference of the ejector thrust force and the external drag force:

$$\text{Propulsive force} = F_{ej} - D_{ex}$$

The secondary air weight flow was computed for each test point by using the total and static pressures and the total temperature measured at a calibrated venturi located in the supply system. Figure 8 shows the variation of the corrected secondary-to-primary weight-flow ratio with jet total-pressure ratio for all test Mach numbers at 0.06 and 0.20 lb/sec of secondary air weight flows.

Accuracy

The estimated accuracy of the data presented in this paper is as follows:

C_p	±0.01
$C_{F,ej}$	±0.01
C_D	±0.01
C_L	±0.005
C_m	±0.001
$\frac{w_s}{w_p}\sqrt{\frac{T_{t,s}}{T_{t,p}}}$	±0.01

The Mach number M was controlled to within ±0.005 and the pressure ratio $p_{t,j}/p_\infty$, to within ±0.1.

RESULTS AND DISCUSSION

Primary-Nozzle Thrust and Flow Coefficients

The variations of w_p/w_i and $C_{F,p}/C_{F_{i,c}}$ with jet total-pressure ratio are shown in figure 9. (The ideal weight flow and the ideal jet thrust of the convergent nozzle are based on measured pressure and temperature.) The data are an average for all Mach numbers at each jet total-pressure ratio. The flow coefficient increases from about 0.92 at $p_{t,j}/p_\infty = 2.0$ to 0.95 at $p_{t,j}/p_\infty = 5.0$, whereas the thrust-coefficient ratio increases from about 0.89 at $p_{t,j}/p_\infty = 2.0$ to 0.95 at $p_{t,j}/p_\infty = 5.0$. These data are low because the convergence angle of the nozzle is 35° (see ref. 12, for example); however, they are in fair agreement with the expected coefficients from convergent nozzles.

Support Interference Effects

The pylon support for the nacelle model is swept back about 73° and is considered to be typical for pylon mounting of jet-engine nacelles in the transonic and low supersonic speed ranges; however, it is recognized that the support would have some interference effects on the model. In order to obtain a qualitative evaluation of the pylon interference effects, afterbody III was also investigated on a sting support system. Inasmuch as it is well known (ref. 13) that a sting may have considerable interference effects on bodies ahead of the support, a third setup was employed. A dummy sting identical to the real sting in the immediate vicinity of the base was attached to the model (see fig. 6) when the model was supported by the pylon.

Figure 10 presents pressure distributions, base pressure coefficients, drag coefficients, and cross-sectional-area distributions for the three types of support system. It is obvious that there is interference present for all types of mounting (figs. 10(a) and 10(b)); however, in practice most multijet nacelle installations are pylon mounted, and interferences similar to those shown herein for the pylon-supported model would be realized. The data for the sting-supported model are another indication of the need for careful evaluation of the support interferences at transonic speeds. Note the significant reduction in the negative pressure peak ($\theta = 0^\circ$ to 90°) and the more positive pressure coefficients over the rearmost sections of the afterbody when compared with the pylon-mounted data. When the dummy sting was installed, the data (figs. 10(a) and 10(b)) did not indicate significant differences from the pylon-mounted data. This result may be an indication that the overall area distribution of the pylon-model combination has a

much larger influence on the afterbody and base pressure than the small additional area of the dummy sting support (fig. 10(d)).

Figure 10(c) presents coefficients of afterbody pressure drag, forebody drag, and external drag (jet off) for the Mach number range of the investigation. The afterbody pressure-drag coefficients for the pylon-supported and pylon-plus-dummy sting are nearly the same at subsonic speeds. At Mach numbers of 1.00 and above, the dummy-sting data indicate a more pronounced interference effect approaching that of the sting-supported values. The forebody drag coefficients and the external-drag coefficients are also affected by support interferences, and the data for both afterbodies I and III indicate a general reduction in drag coefficient with the sting support.

Interference data taken from reference 13 and applied to the sting-mounted model indicated that an interference-free model with afterbody III would have substantially the same external-drag coefficients as were measured by the pylon-supported model. This result may be fortuitous in that the area-distribution differences may act in a compensating manner. It is estimated, however, that the pylon-supported-model data fairly represent a practical nacelle installation in spite of an unknown interference effect of the pylon.

Afterbody-Pressure Distributions

Effect of secondary air flow on afterbody pressures.- Figure 11 presents pressure-coefficient data at station $x/l = 0.987$ for 0, 0.06, and 0.20 lb/sec of secondary air flow. Station $x/l = 0.987$ was chosen because it was estimated that the largest effects would be shown here. The addition of 0.20 lb/sec of secondary air flow acts in the manner of base bleed for the jet-off cases at both Mach numbers, inasmuch as the pressure coefficients become more positive. This is a typical result of the addition of base-bleed flow (see refs. 1 and 14). When the jet is operating at a jet total-pressure ratio of 4.0, the effect on the pressures is generally the same as when the jet is off, except for afterbody I at $M = 1.05$, where the addition of 0.20 lb/sec of secondary air was detrimental. This detrimental effect is probably the result of increased jet pumping on the separated flow over the 28° conical boattail.

Effect of jet total-pressure ratio on afterbody pressure distributions.- Pressure distributions over afterbodies I, II, and III are shown in figures 12, 13, and 14, respectively, for several Mach numbers and nominal values of jet total-pressure ratio. It should be noted that the data in figure 14 are presented for $w_s = 0.20$ lb/sec, and this value has been shown in figure 11 to have a small beneficial effect. The data for afterbody I indicate that increasing jet total-pressure ratio had a relatively small effect on the level of the pressure coefficients

on the afterbody. In general, the slight effect noted was to make the pressures more negative; reference 4 indicates a similar trend for a 30° conical boattail. Jet operation has a beneficial effect on afterbody II, with the negative peak at $x/l = 0.60$ being reduced and the point of $C_p = 0$ being moved to lower values of x/l when the jet pressure ratio is increased. Similar pressure distributions and jet effects have been observed previously. (For example, see refs. 3 and 4.)

Comparison of figures 13 and 14 indicates that the generous radius applied to the sharp corner at the start of the conical afterbody reduces the magnitude of the negative pressure peak. Jet operation further reduces the negative pressure peak and the positive pressure region generally becomes larger. An example of the movement of the afterbody shock forward on the boattail is shown in the shadowgraph pictures of figure 15. The forward movement of the shock results from jet interference with the external flow and produces a larger positive pressure region on the afterbody with increasing jet total-pressure ratio. Mach number has a small effect on the pressure distributions; however, a tendency for the pressure peak to become more negative with increasing Mach number is noted for afterbody III, whereas the opposite trend occurs for afterbody II.

Effect of jet total-pressure ratio on afterbody drag coefficient.- The variation of afterbody pressure-drag coefficient with jet total-pressure ratio is shown in figure 16 for several Mach numbers and secondary air weight flows. These data were obtained by integrating the pressure distributions shown previously. It is noted that the effect of jet operation is generally detrimental on afterbody I, the 28° boattail, and beneficial on afterbodies II and III, the 15° boattails. Where larger quantities of secondary air flow were used, the afterbody pressure-drag coefficient decreased for all jet total-pressure ratios below 5.0. Calculation of the jet boundary by the method of reference 15 indicated that the primary jet would impinge on the conical ejector at jet total-pressure ratios of about 5.0. This impingement was noted in the data when the secondary air pressures and temperatures suddenly increased. The consequent mixing of the primary and secondary flows inside the ejector would eliminate the base-bleed effect of the secondary flow and no significant effect of these quantities of secondary flow would be expected at jet total-pressure ratios of 5.0 and above. This impingement effect would be modified in the case of an actual installation, inasmuch as the ejector would probably be opened to at least partial afterburning near a jet total-pressure ratio of 5.0.

Aerodynamic Characteristics

The variation of external-drag coefficient with jet total-pressure ratio for several Mach numbers and secondary air weight flows is shown

in figure 17. As would be expected, the results are similar to those noted previously for the afterbody drag, since external-drag coefficient is the sum of the forebody drag coefficient presented in figure 7 and the afterbody pressure-drag coefficient presented in figure 16. It is noted that afterbody III has the lowest external-drag coefficient of the afterbodies investigated over most of the Mach number and jet total-pressure ratio ranges.

Figure 18 shows the variation of lift coefficient C_L and pitching-moment coefficient C_m with jet total-pressure ratio for several Mach numbers. The variations shown with increasing jet total-pressure ratio are estimated to be due to misalinement of the primary jet in the ejector nozzle because integration of the afterbody pressures for normal force shows that only a small part (15 percent) of the variation is the result of external effects. It was noted in all cases where large variations occur that the internal pressures on one side of the ejector were considerably more positive than on the other, and this fact is an indication that the primary jet was washing one wall and not the other. No particular significance is attached to this condition; however, it serves to point out the magnitude of the asymmetrical loads that can be obtained if the primary stream is not centered in the ejector.

Performance Characteristics

The variation of ejector thrust and ideal thrust coefficients with primary jet total-pressure ratio of the three afterbody configurations is shown in figure 19 for all test Mach numbers. It can be seen that the ejector thrust coefficient increased uniformly with primary jet total-pressure ratio and indicated no sudden losses associated with jet attachment. The addition of 0.20 lb/sec of secondary air flow increased the ejector thrust to values obtained with the primary nozzle alone. It is noted that the addition of 0.06 lb/sec of secondary air flow had very little effect on the ejector thrust. The reason that 0.06 lb/sec of secondary air flow has such a small effect is probably due to the low total pressure of the secondary flow.

The performance of the ejectors and afterbodies is shown in figure 20 as variations in ejector jet thrust ratio and afterbody pressure-drag coefficient over the Mach number range of the investigation. The performance is presented at the scheduled pressure ratio for each Mach number shown in figure 20. This variation of pressure ratio with Mach number is considered to be typical for turbojet engines with subsonic-cruise—supersonic-dash capabilities. The general level of the ejector jet thrust ratio is of the order expected and the decrease in ejector thrust ratio of about 0.02 from afterbody I to afterbodies II and III is of the order indicated by the results of reference 5. (Note that

jet thrust ratios of afterbodies II and III are identical above a Mach number of 0.90.)

Afterbody III, which had a smooth transition to the 15° boattail angle, had the lowest external-drag coefficient over the Mach number range of the investigation. In order to evaluate the relative performance of the three configurations, plots of ejector thrust coefficient minus external-drag coefficient are presented in figure 21. The thrust-minus-drag performance of afterbody III was the best of the afterbodies investigated and shows that the design of an ejector should be integrated with the afterbody design to obtain the maximum overall gains in performance, even though the ejector may not be optimum.

CONCLUSIONS

An investigation of a pylon-supported nacelle model with three afterbody-ejector configurations has been conducted in the Langley 16-foot transonic tunnel at an angle of attack of 0° over a Mach number range from 0.80 to 1.05. The results of the investigation have led to the following conclusions:

1. The jet effect on afterbody I, which had a 28° boattail angle, was generally detrimental and intensified with increasing Mach number.

2. The jet effect on afterbodies II and III, which had 15° boattail angles, was beneficial and generally similar for both afterbodies.

3. Afterbody III, which had a smooth transition to the 15° boattail angle, had the lowest external-drag coefficient over the Mach number range.

4. The increase in ejector spacing ratio from afterbody I to afterbody III resulted in a loss of about 0.02 in ejector jet thrust ratios; however, the thrust-minus-drag performance of afterbody III was the best of the afterbodies investigated and shows that the design of an ejector should be integrated with the afterbody design to obtain the maximum overall performance.

Langley Research Center,
National Aeronautics and Space Administration,
Langley Field, Va., October 8, 1958.

REFERENCES

1. Salmi, Reino J.: Experimental Investigation of Drag of Afterbodies With Exiting Jet at High Subsonic Mach Numbers. NACA RM E54I13, 1954.

2. Henry, Beverly Z., Jr., and Cahn, Maurice S.: Preliminary Results of an Investigation at Transonic Speeds To Determine the Effects of a Heated Propulsive Jet on the Drag Characteristics of a Related Series of Afterbodies. NACA RM L55A24a, 1955.

3. Henry, Beverly Z., Jr., and Cahn, Maurice S.: Pressure Distributions Over a Series of Related Afterbody Shapes As Affected by a Propulsive Jet at Transonic Speeds. NACA RM L56K05, 1957.

4. Cubbage, James M., Jr.: Jet Effects on the Drag of Conical Afterbodies for Mach Numbers of 0.6 to 1.28. NACA RM L57B21, 1957.

5. Greathouse, W. K., and Hollister, D. P.: Preliminary Air-Flow and Thrust Calibrations of Several Conical Cooling-Air Ejectors With a Primary to Secondary Temperature Ratio of 1.0. I - Diameter Ratios of 1.21 and 1.10. NACA RM E52E21, 1952.

6. Greathouse, W. K., and Hollister, D. P.: Preliminary Air-Flow and Thrust Calibrations of Several Conical Cooling-Air Ejectors With a Primary to Secondary Temperature Ratio of 1.0. II - Diameter Ratios of 1.06 and 1.40. NACA RM E52F26, 1952.

7. Greathouse, W. K.: Preliminary Investigation of Pumping and Thrust Characteristics of Full-Size Cooling-Air Ejectors at Several Exhaust-Gas Temperatures. NACA RM E54A18, 1954.

8. Stitt, Leonard E., and Valerino, Alfred S.: Effect of Free-Stream Mach Number on Gross-Force and Pumping Characteristics of Several Ejectors. NACA RM E54K23a, 1955.

9. Cubbage, James M., Jr.: Effect of Convergent Ejector Nozzles on the Boattail Drag of a 16° Conical Afterbody at Mach Numbers of 0.6 to 1.26. NACA RM L58G25, 1958.

10. Runckel, Jack F., and Swihart, John M.: A Hydrogen Peroxide Hot-Jet Simulator for Wind-Tunnel Tests of Turbojet-Exit Models. NASA MEMO 1-10-59L, 1959.

11. Runckel, Jack F.: Preliminary Transonic Performance Results for Solid and Slotted Turbojet Nacelle Afterbodies Incorporating Fixed Divergent Jet Nozzles Designed for Supersonic Operation. NASA MEMO 10-24-58L, 1958.

12. Krull, H. George, and Beale, William T.: Internal Performance Characteristics of Short Convergent-Divergent Exhaust Nozzles Designed by the Method of Characteristics. NACA RM E56D27a, 1956.

13. Cahn, Maurice S.: An Experimental Investigation of Sting-Support Effects on Drag and a Comparison With Jet Effects at Transonic Speeds. NACA Rep. 1353, 1958. (Supersedes NACA RM L56F18a.)

14. Cortright, Edgar M., Jr., and Schroeder, Albert H.: Preliminary Investigation of Effectiveness of Base Bleed in Reducing Drag of Blunt-Base Bodies in Supersonic Stream. NACA RM E51A26, 1951.

15. Love, Eugene S., Grigsby, Carl E., Lee, Louise P., and Woodling, Mildred J.: Experimental and Theoretical Studies of Axisymmetric Free Jets. NASA TR R-6, 1959. (Supersedes NACA RM L54L31 by Love and Grigsby, RM L55J14 by Love, RM L56G18 by Love, Woodling, and Lee, and TN 4195 by Love and Lee.)

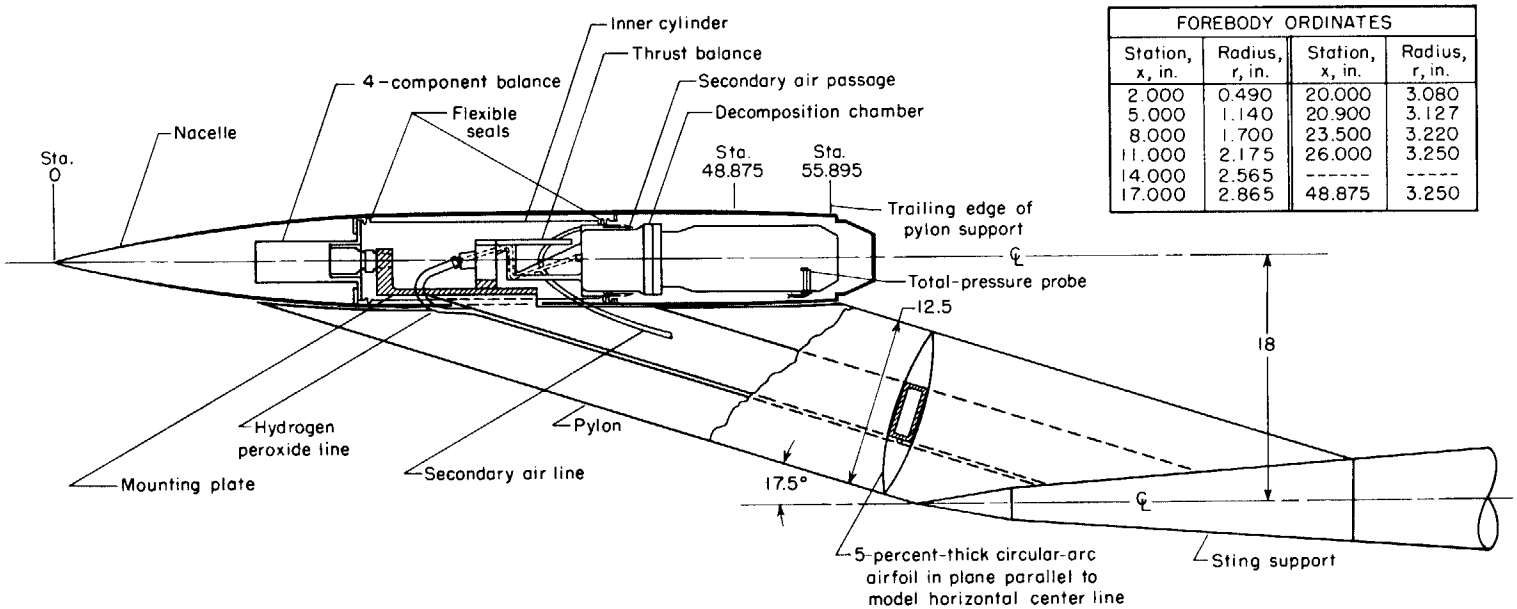

FOREBODY ORDINATES			
Station, x, in.	Radius, r, in.	Station, x, in.	Radius, r, in.
2.000	0.490	20.000	3.080
5.000	1.140	20.900	3.127
8.000	1.700	23.500	3.220
11.000	2.175	26.000	3.250
14.000	2.565	------	-----
17.000	2.865	48.875	3.250

Figure 1.- Sketch of pylon-supported nacelle turbojet-engine simulator model. (All dimensions are in inches.)

Figure 2.- Pylon-supported nacelle model with afterbody I installed. L-57-2524

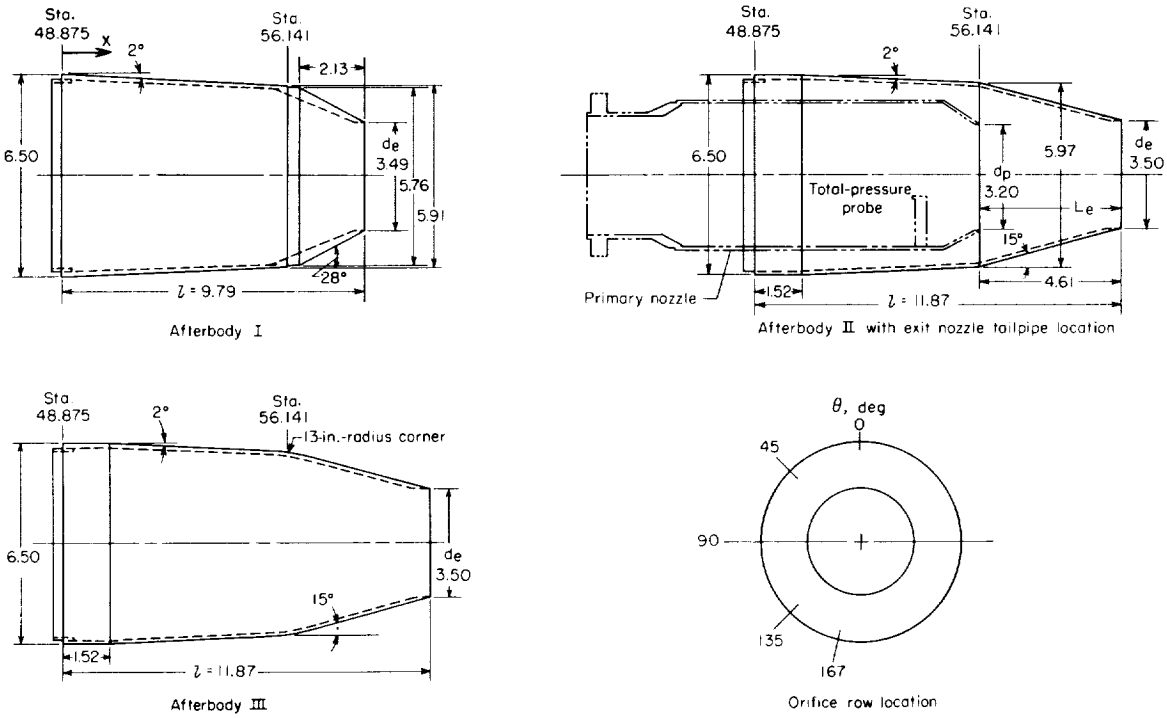

Note: Primary-nozzle exit at station 56.141 for all afterbodies.

EJECTOR GEOMETRY		
Afterbody	Exit-to-jet-diameter ratio, d_e/d_p	Spacing ratio, L_e/d_p
I	1.091	0.789
II	1.094	1.440
III	1.094	1.440

EXTERNAL ORIFICE LOCATIONS					
Afterbody I			Afterbodies II and III		
Row	x	x/l	Row	x	x/l
θ = 0°, 45°, 90°, 135°, and 167°	0.731	0.075	θ = 0°, 45°, 90°, 135°, and 167°	2.254	0.190
	2.836	.290		3.925	.331
	4.941	.505		5.585	.470
	7.046	.720		7.141	.601
	7.266	.742		7.391	.622
	7.658	.782		8.256	.695
	7.909	.808		9.121	.768
	8.411	.859		9.986	.841
	8.913	.910		10.851	.914
	9.415	.962		11.716	.987
	9.666	.987			

INTERNAL ORIFICE LOCATIONS					
Afterbody I			Afterbodies II and III		
Primary-nozzle flap					
Row	x	x/l	Row	x	x/l
θ = 0°, and 180°	6.124	0.625	θ = 0° and 180°	6.124	0.516
	6.644	.678		6.644	.560
	7.174	.733		7.174	.604
Ejector wall					
Row	x	x/l	Row	x	x/l
θ = 18° and 180°	8.473	.865	θ = 18° and 180°	8.374	.705
	8.973	.916		9.874	.832
	9.473	.967		11.174	.941
				11.674	.983

Figure 3.- Sketch of afterbody configurations and locations of pressure orifices. (All dimensions are in inches.)

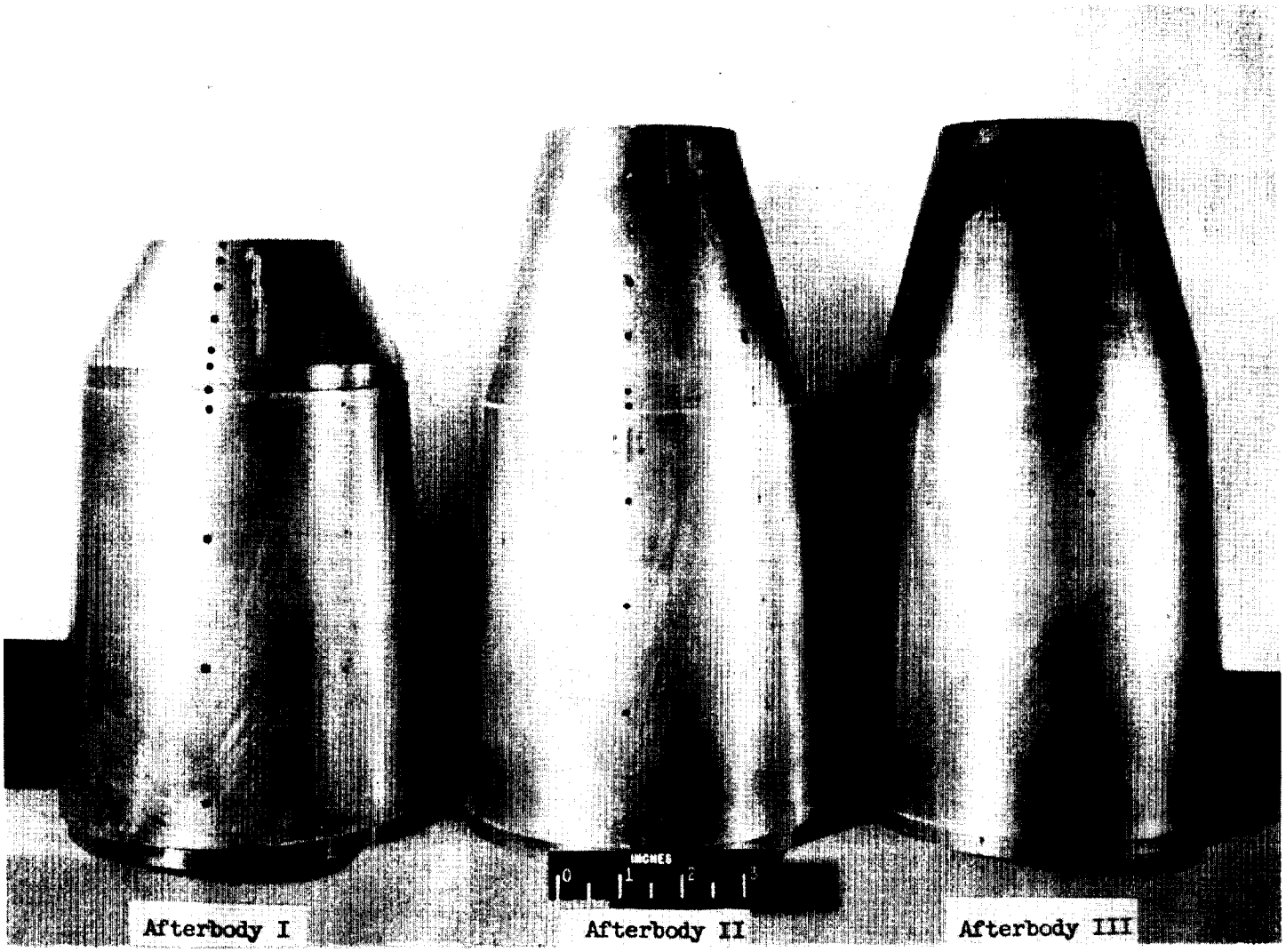

Figure 4.- Photograph of the afterbody configurations. L-58-621.1

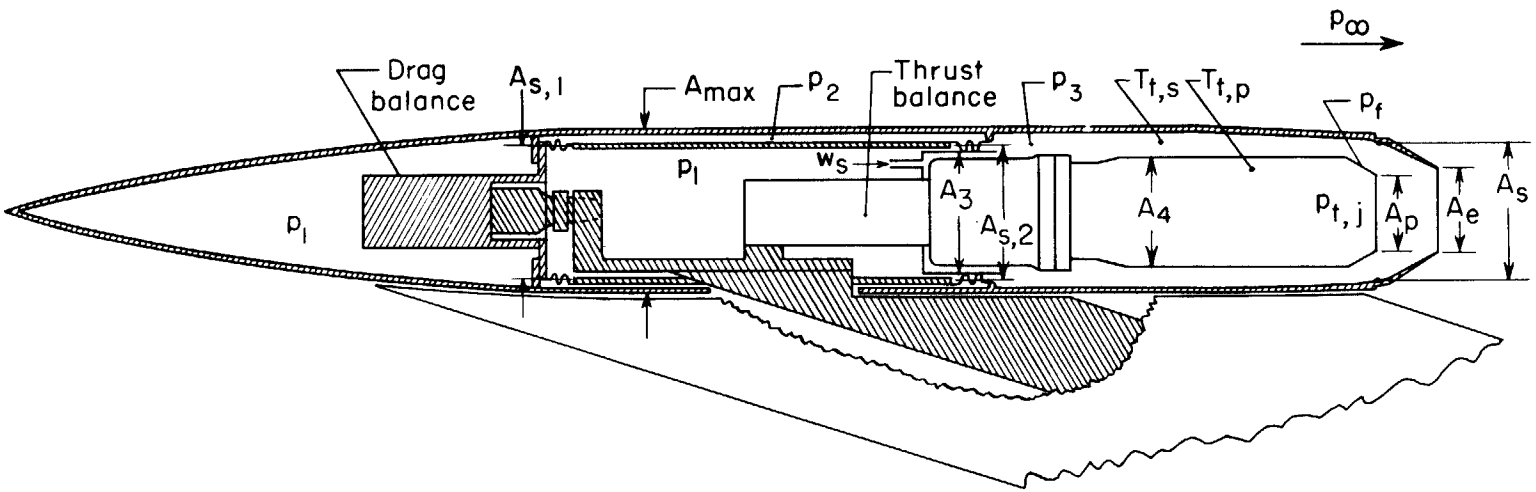

Figure 5.- Schematic diagram showing thrust and drag systems.

(a) Pylon mounted.

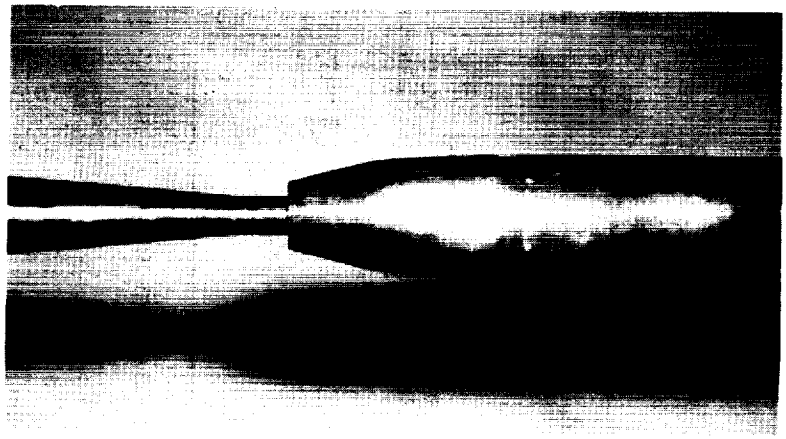

(b) Sting mounted.

(c) Pylon mounted with dummy sting. L-58-109a

Figure 6.- Photograph of afterbody III mounted in tunnel test section.

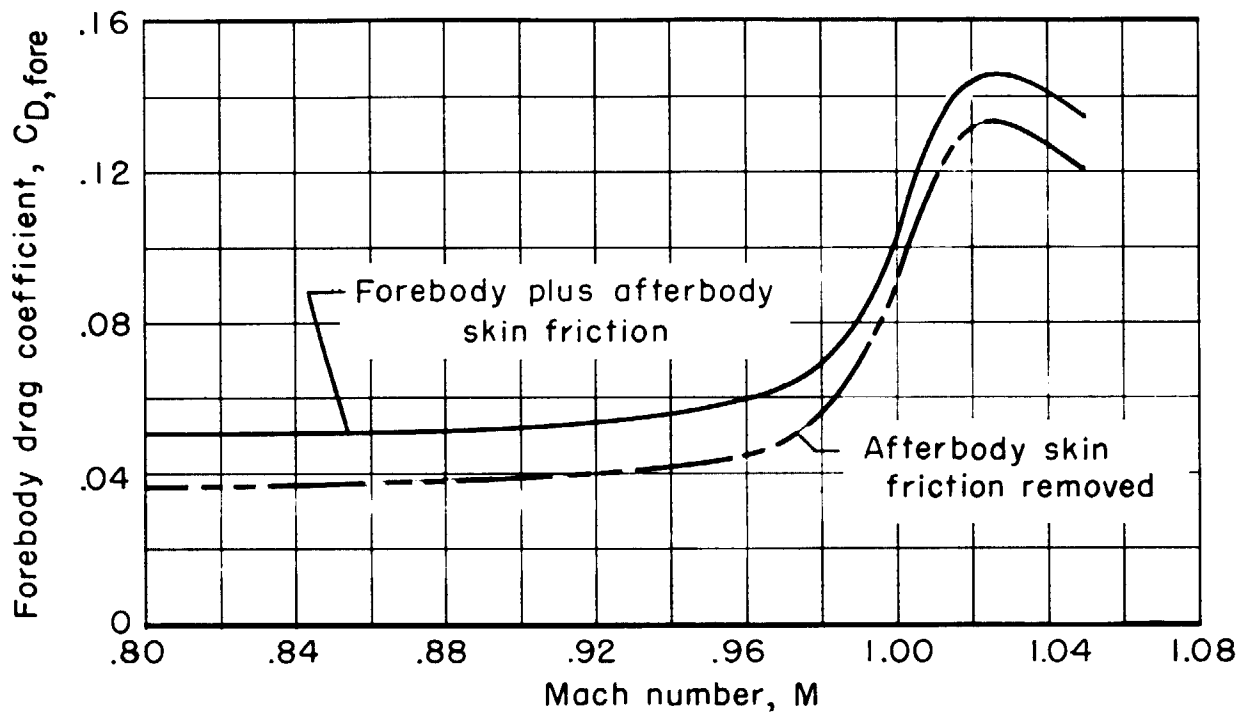

Figure 7.- Effect of Mach number on forebody drag coefficient of pylon-supported nacelle. Jet off.

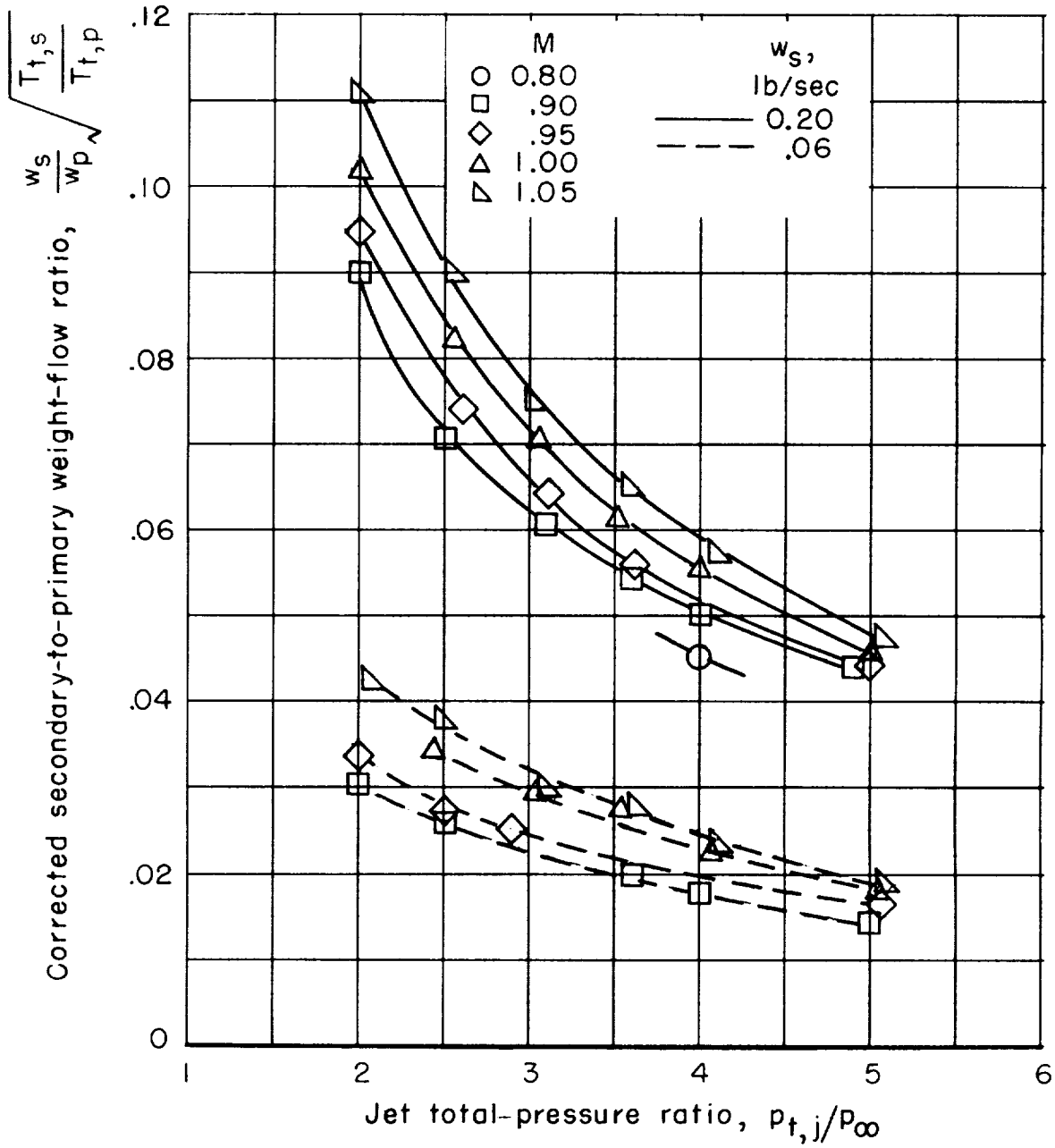

Figure 8.- Variation of corrected secondary-to-primary weight-flow ratio with jet total-pressure ratio for all test Mach numbers.

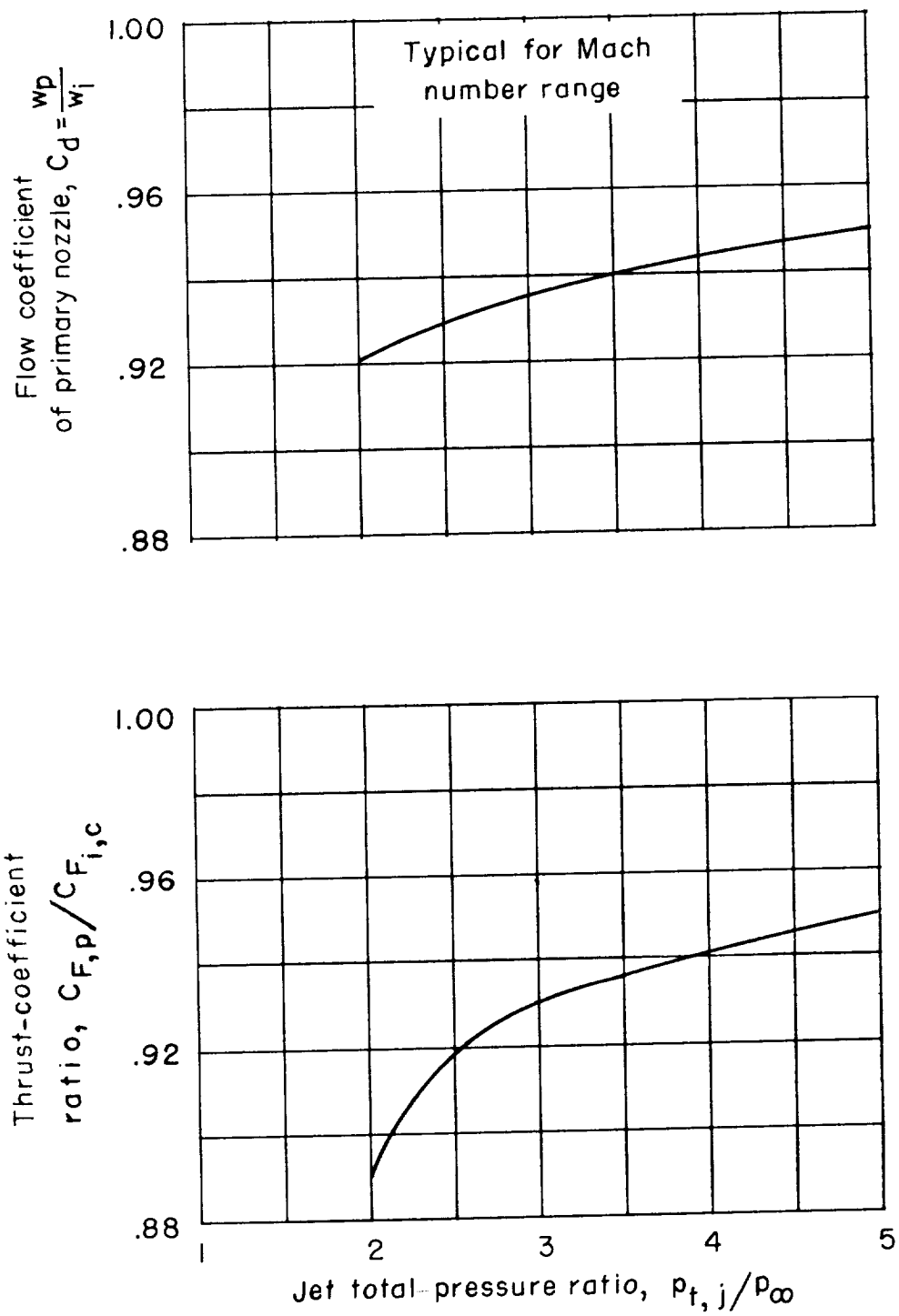

Figure 9.- Thrust and flow coefficients for the primary nozzle.

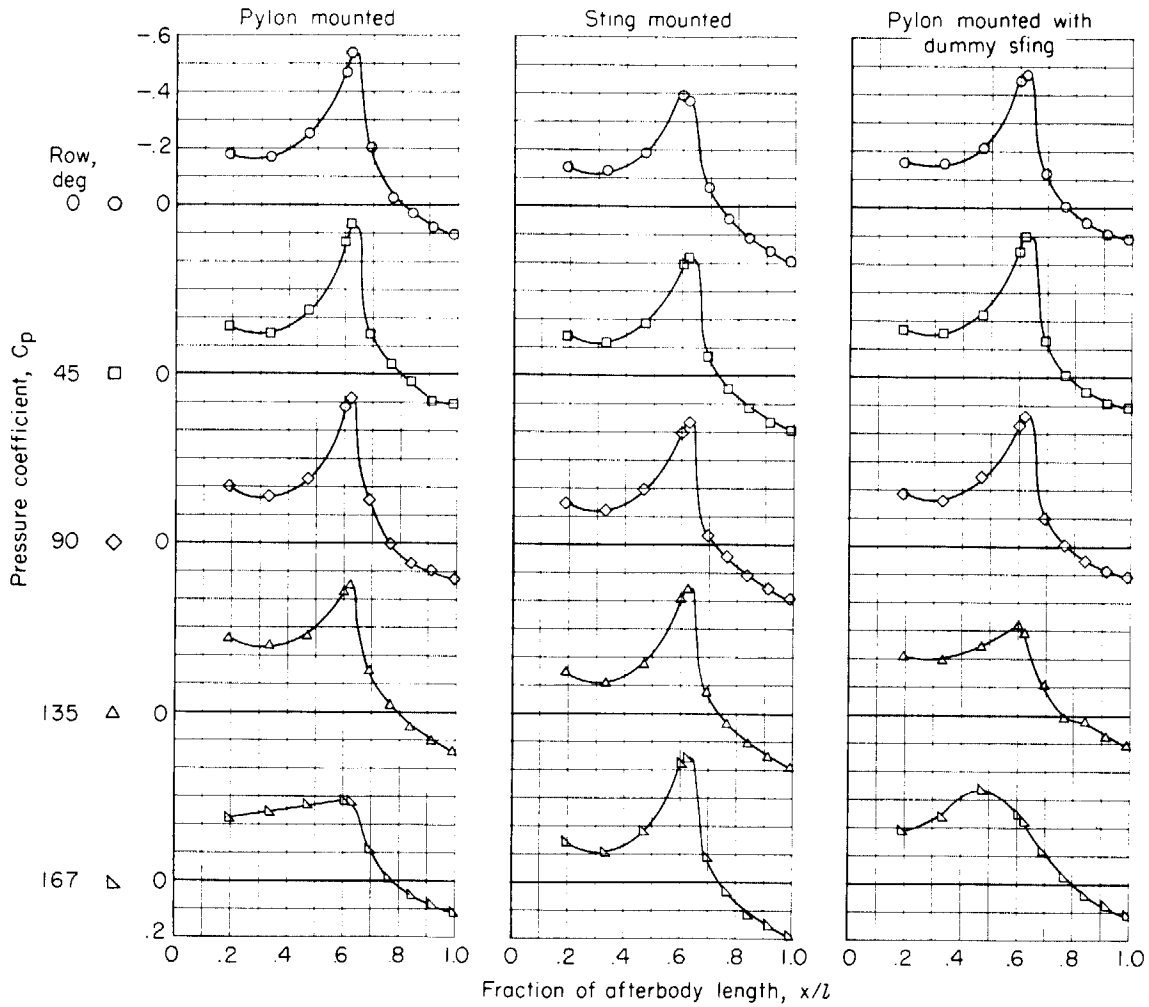

(a) Afterbody III pressure distributions at M = 0.90.

Figure 10.- Evaluation of support interference effects. Jet off.

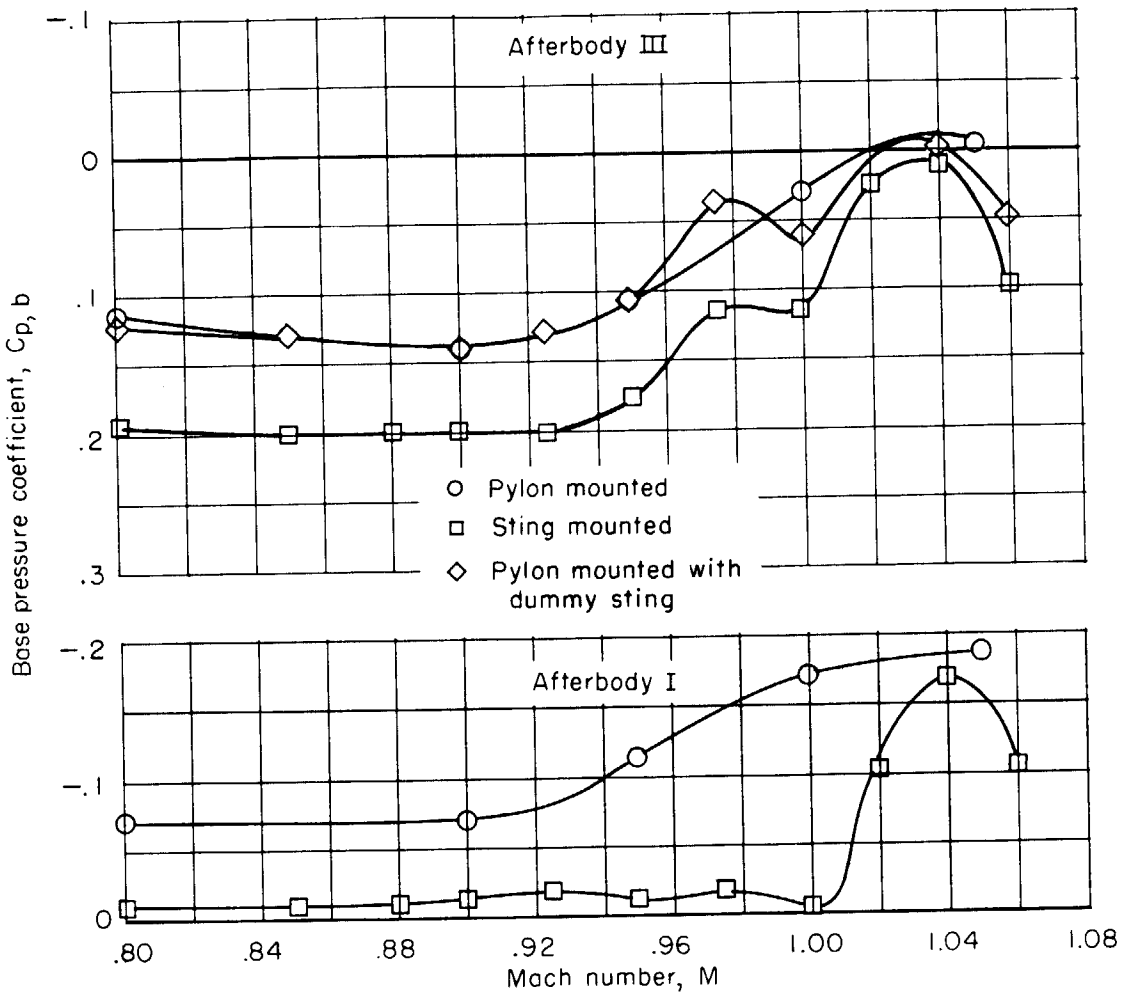

(b) Base pressure coefficients.

Figure 10.- Continued.

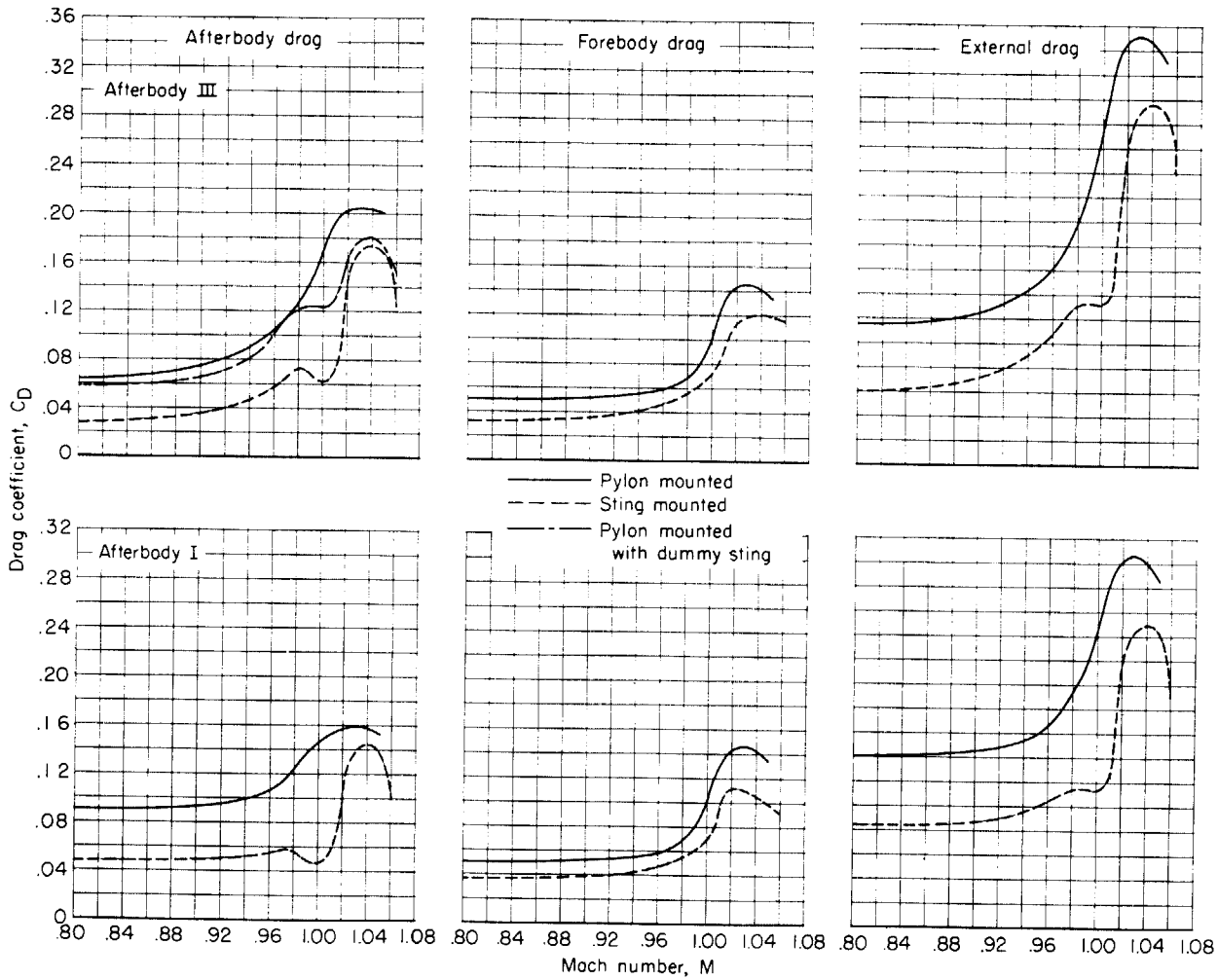

(c) Drag coefficients.

Figure 10.- Continued.

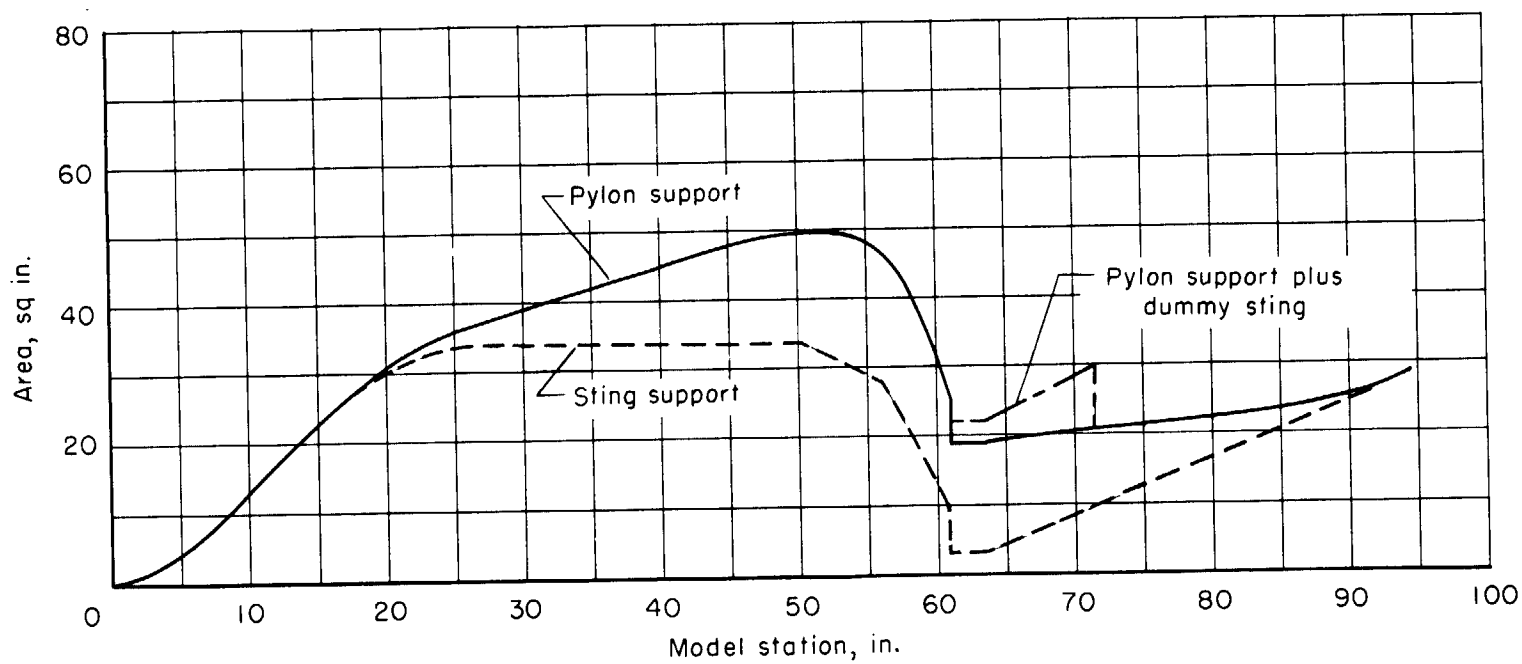

(d) M = 1.00 area distribution of nacelle and support system.

Figure 10.- Concluded.

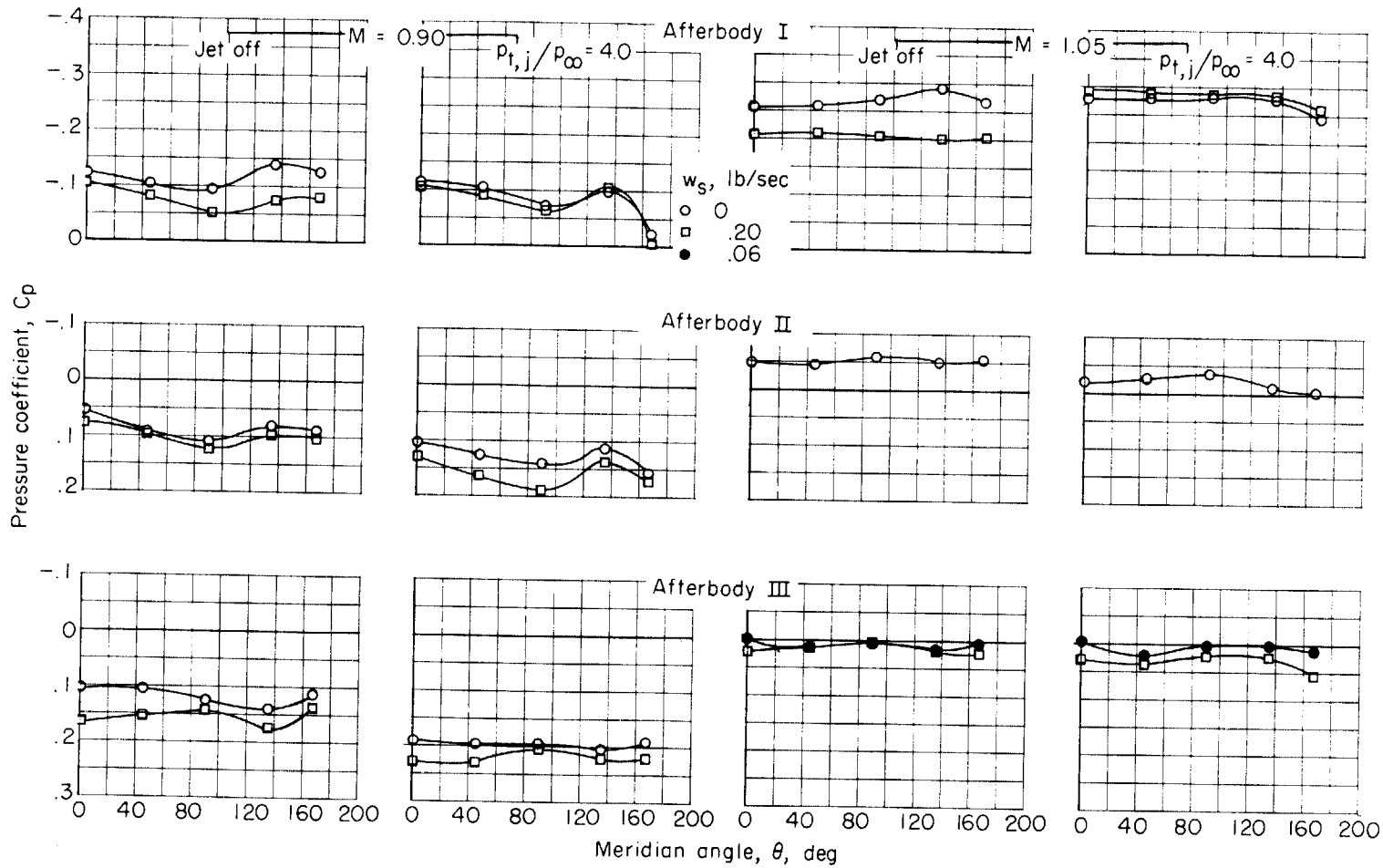

Figure 11.- Effect of secondary air flow on peripheral afterbody pressure coefficients at x/l = 0.987.

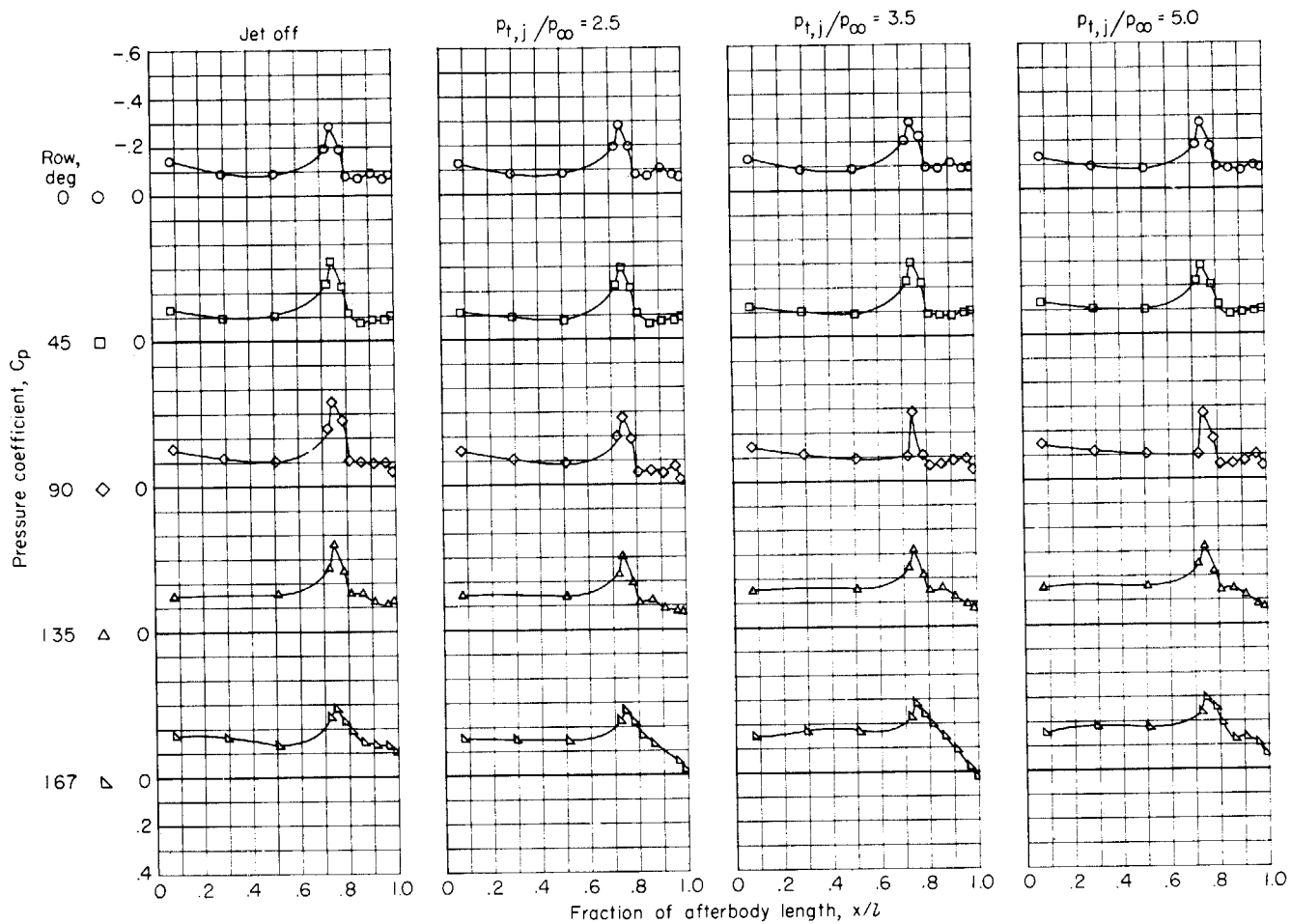

(a) M = 0.80.

Figure 12.- Effect of jet total-pressure ratio on afterbody I pressure distributions. w_s = 0 lb/sec.

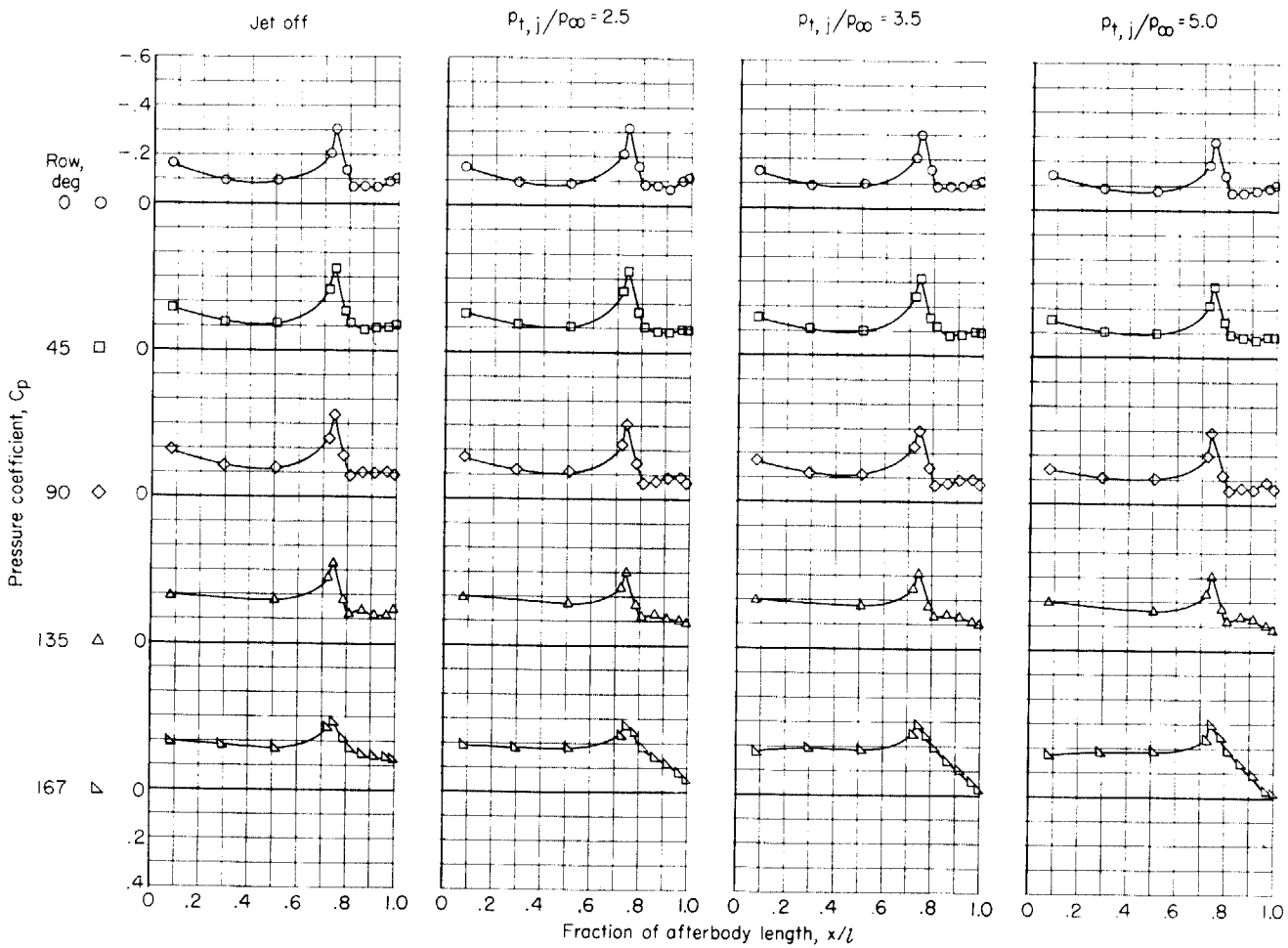

(b) M = 0.90.

Figure 12.- Continued.

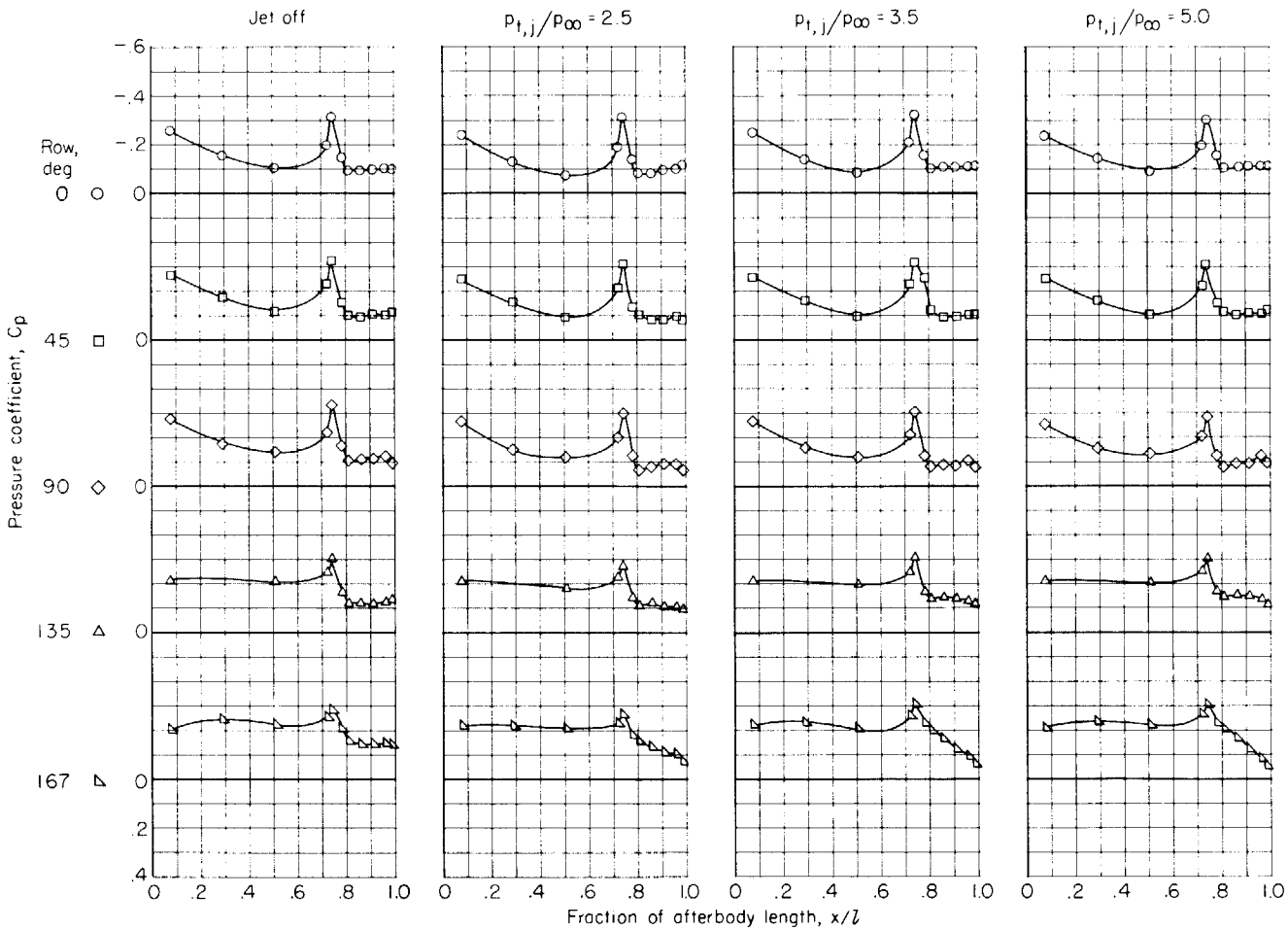

(c) M = 0.95.

Figure 12.- Continued.

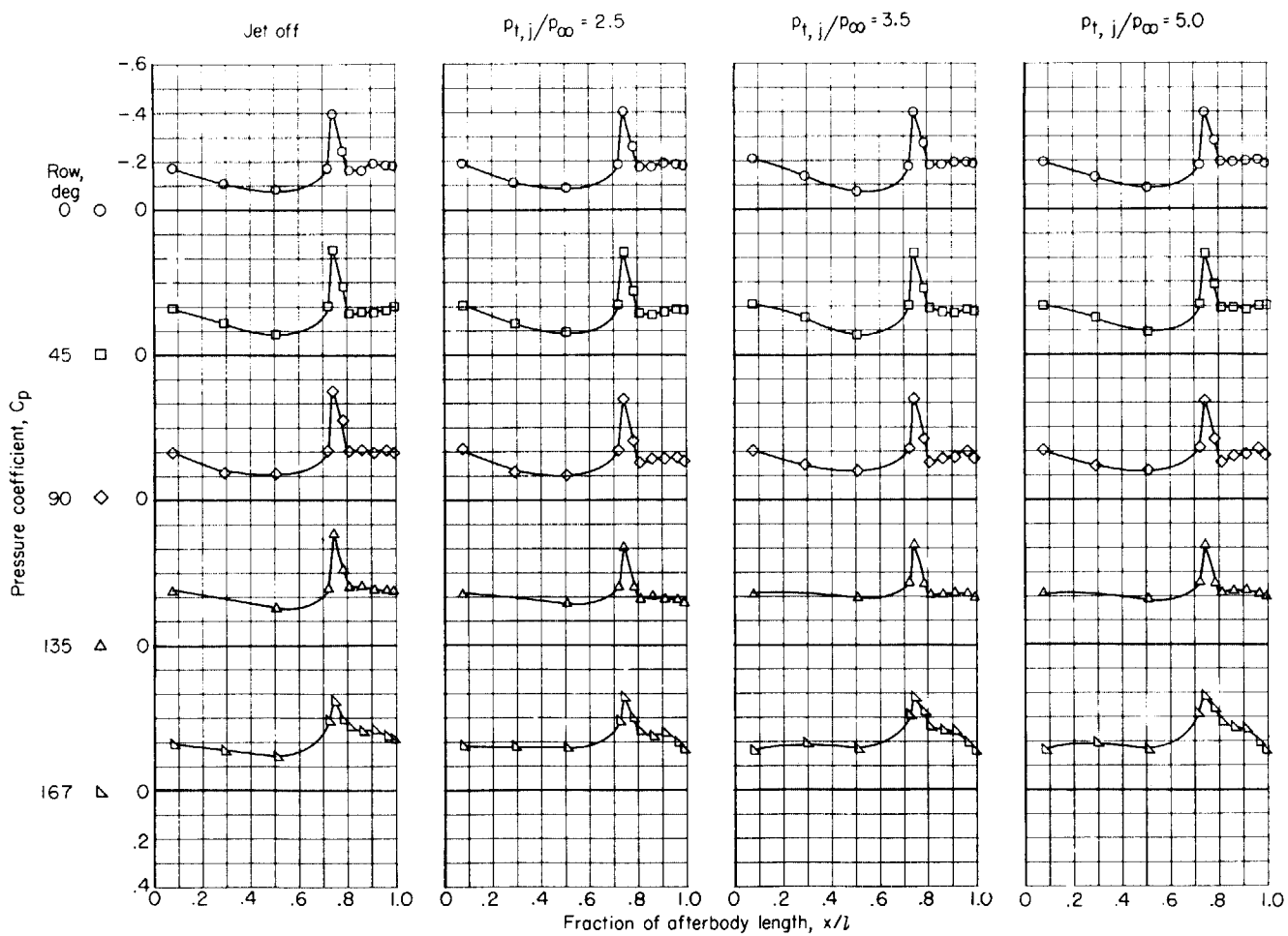

(d) M = 1.00.

Figure 12.- Continued.

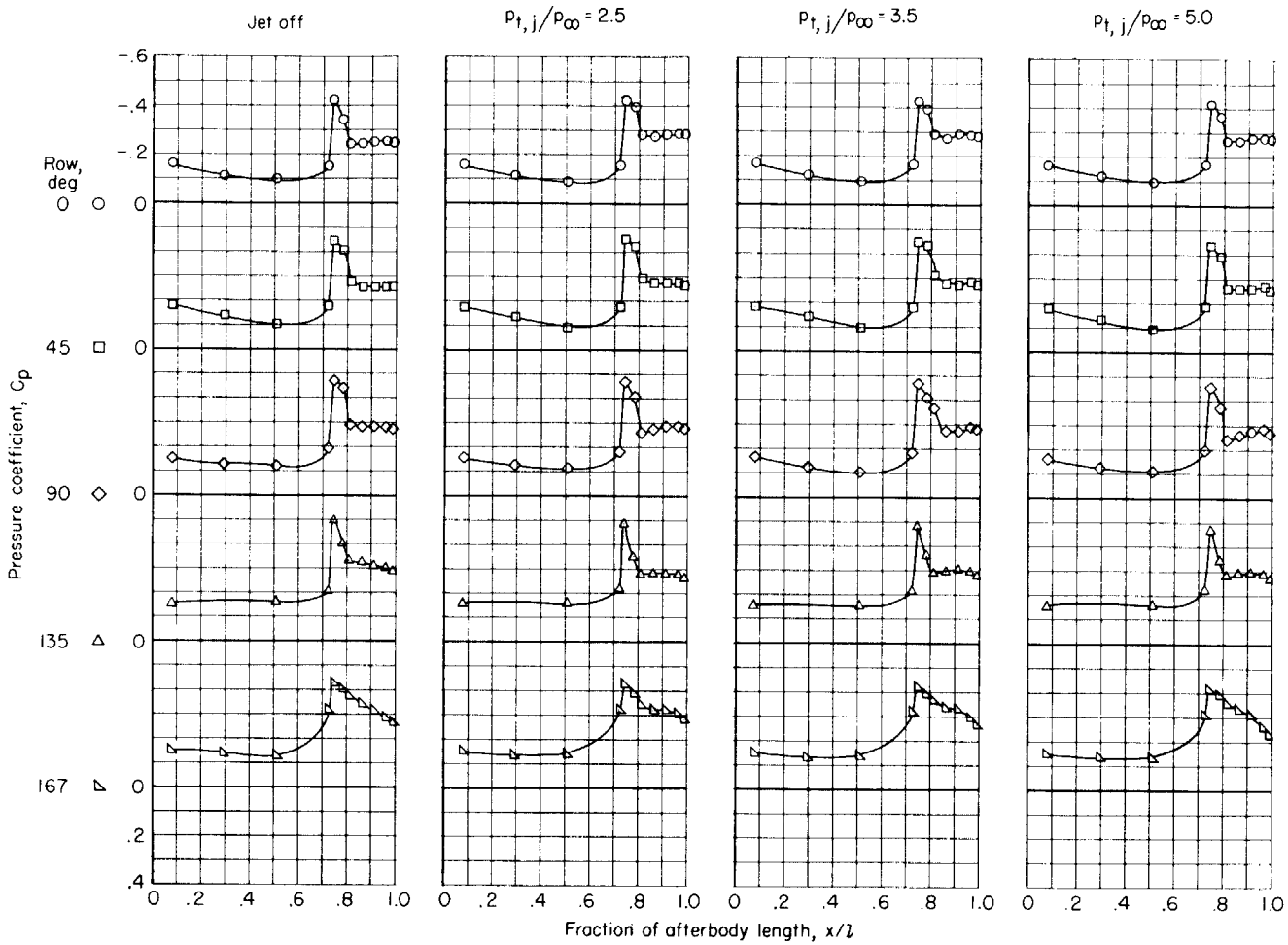

(e) M = 1.05.

Figure 12.- Concluded.

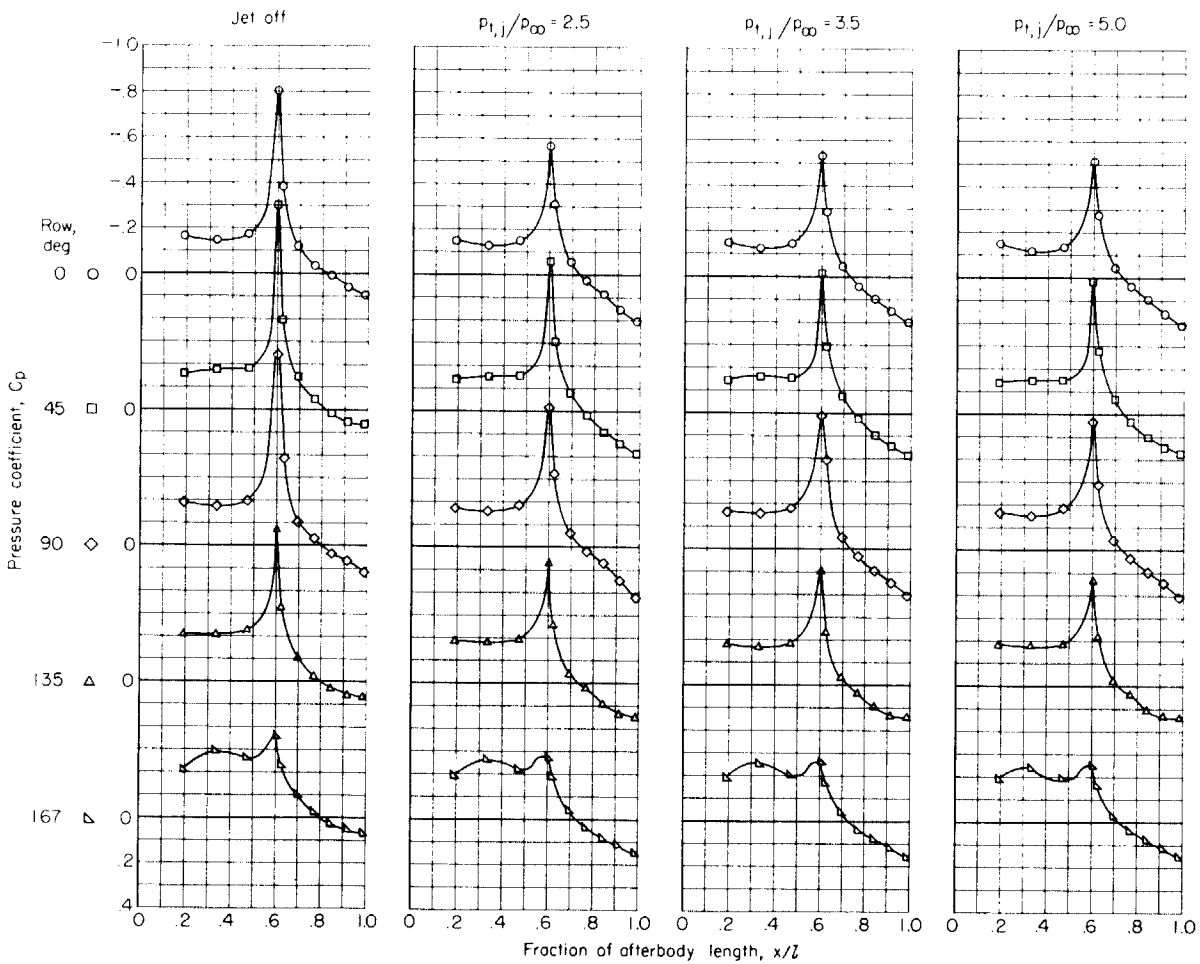

(a) M = 0.80.

Figure 13.- Effect of jet total-pressure ratio on afterbody II pressure distributions. w_s = 0 lb/sec.

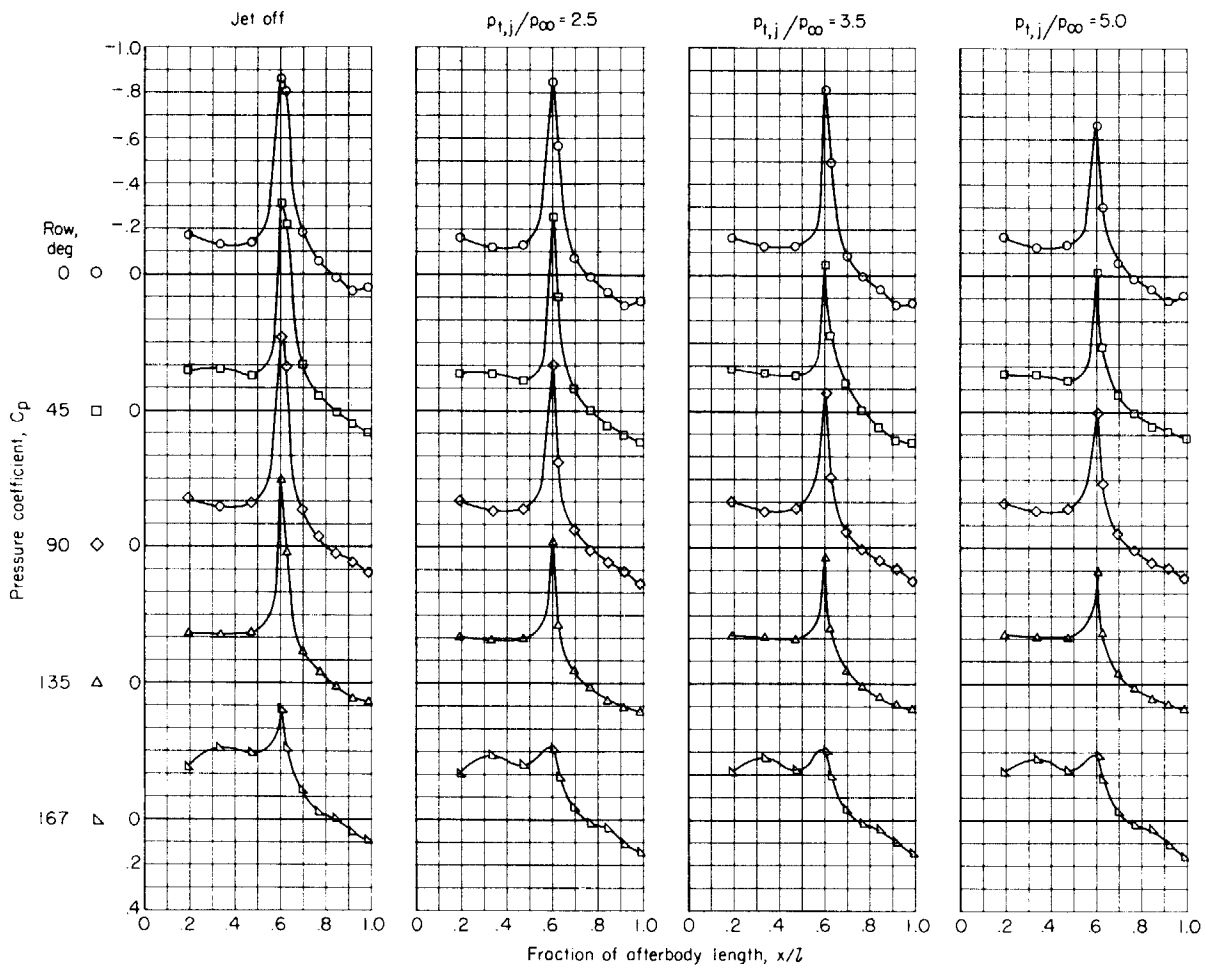

(b) M = 0.90.

Figure 13.- Continued.

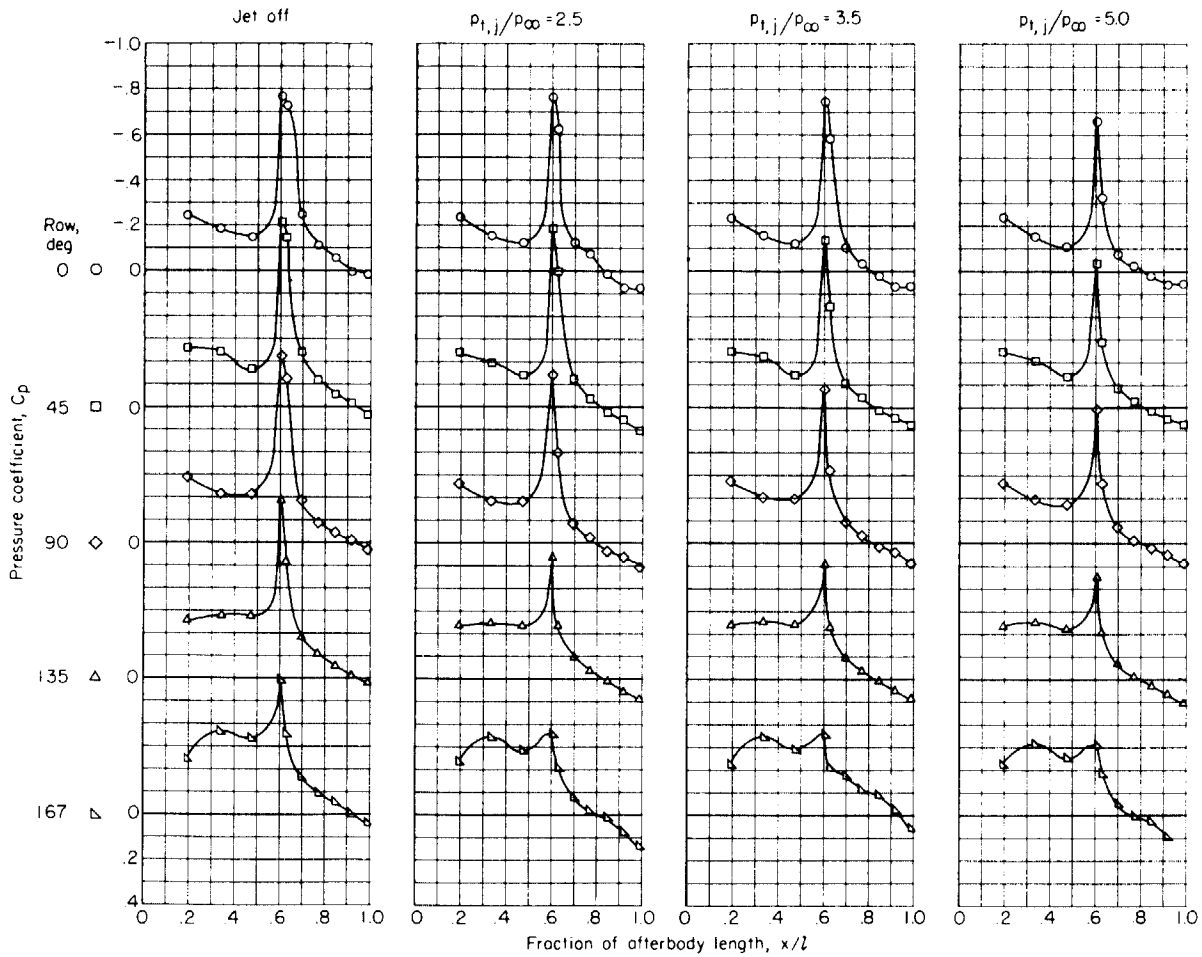

(c) M = 0.95.

Figure 13.- Continued.

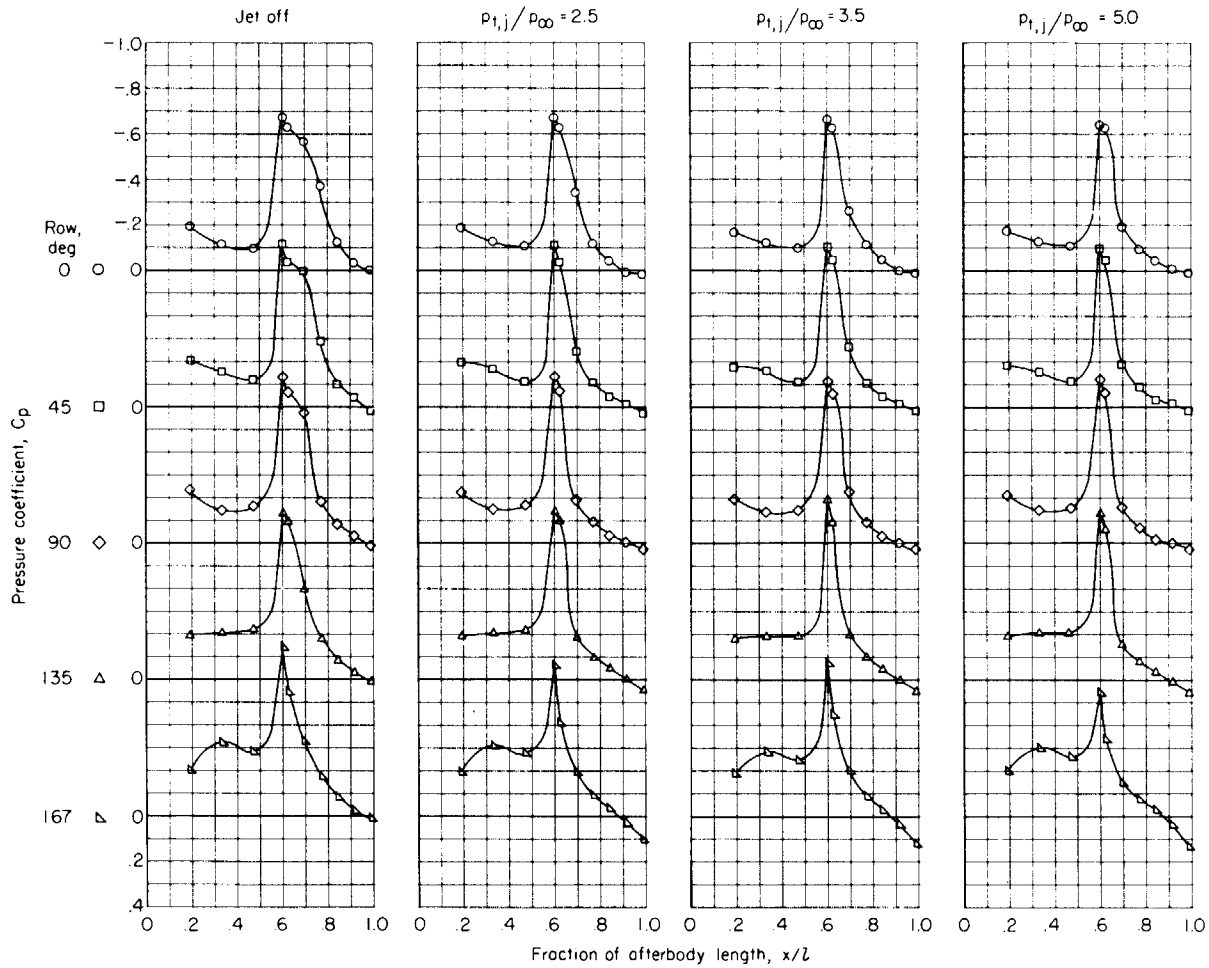

(d) M = 1.00.

Figure 13.- Continued.

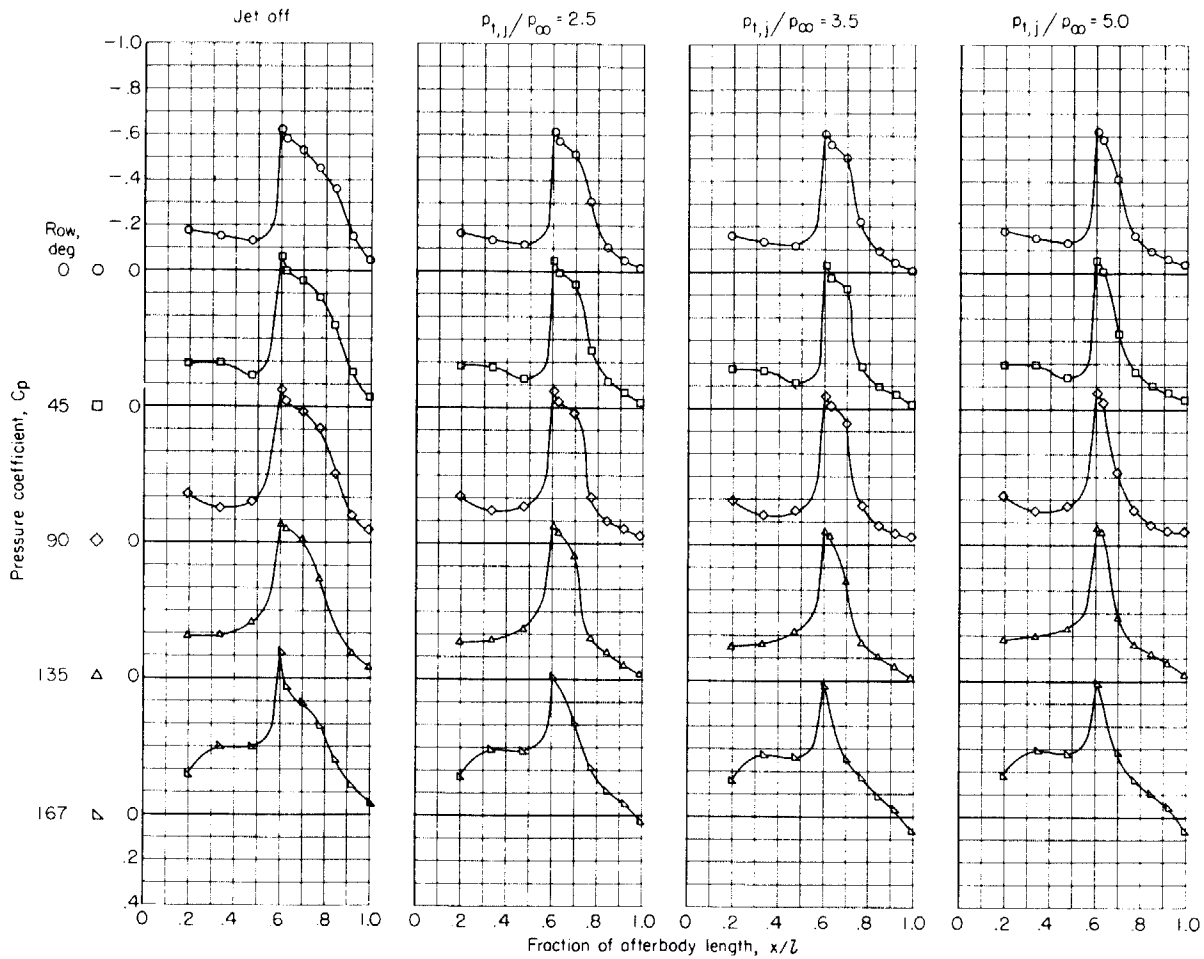

(e) M = 1.05.

Figure 13.- Concluded.

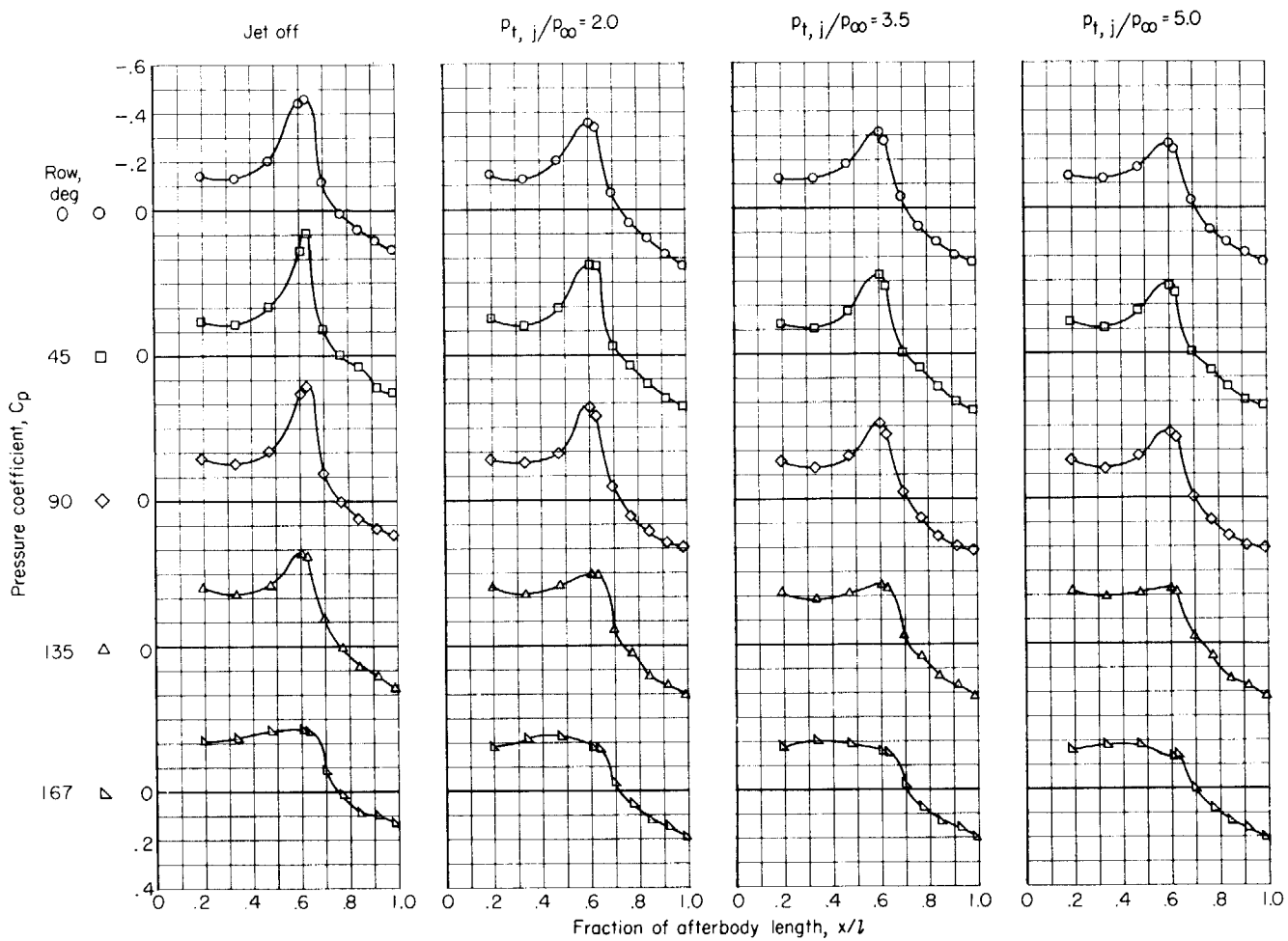

(a) M = 0.90.

Figure 14.- Effect of jet total-pressure ratio on afterbody III pressure distributions. w_s = 0.20 lb/sec.

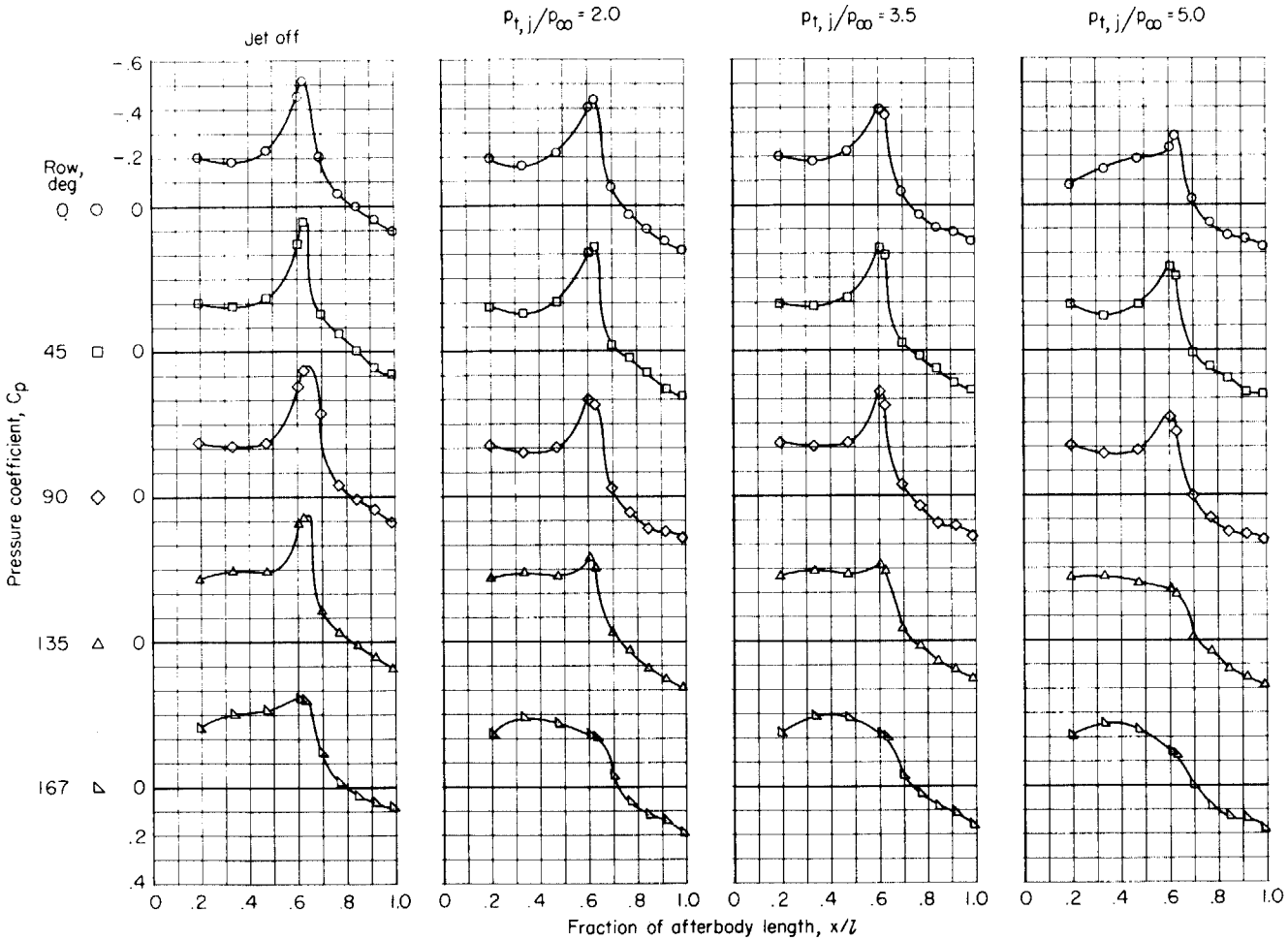

(b) M = 0.95.

Figure 14.- Continued.

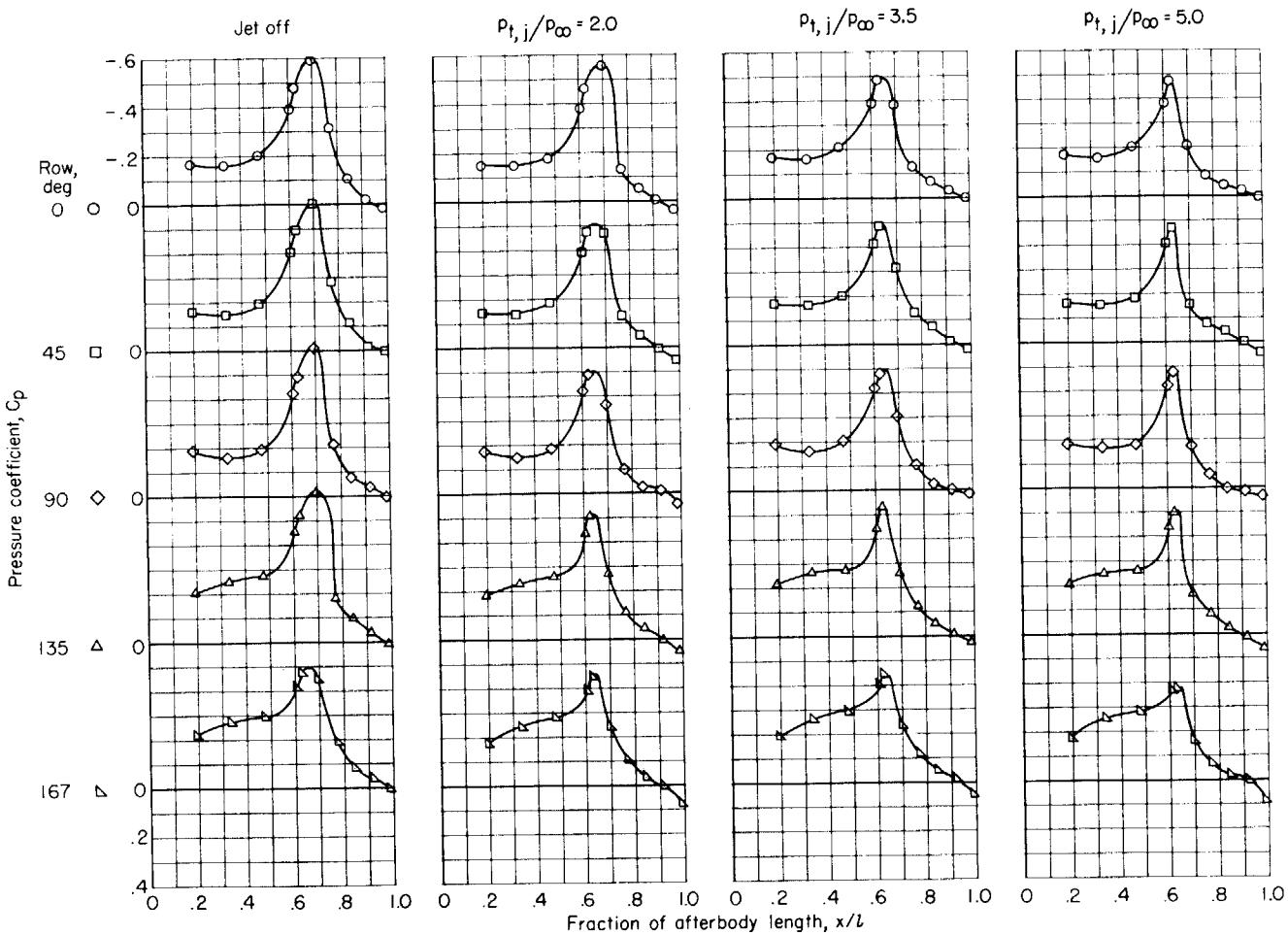

(c) M = 1.00.

Figure 14.- Continued.

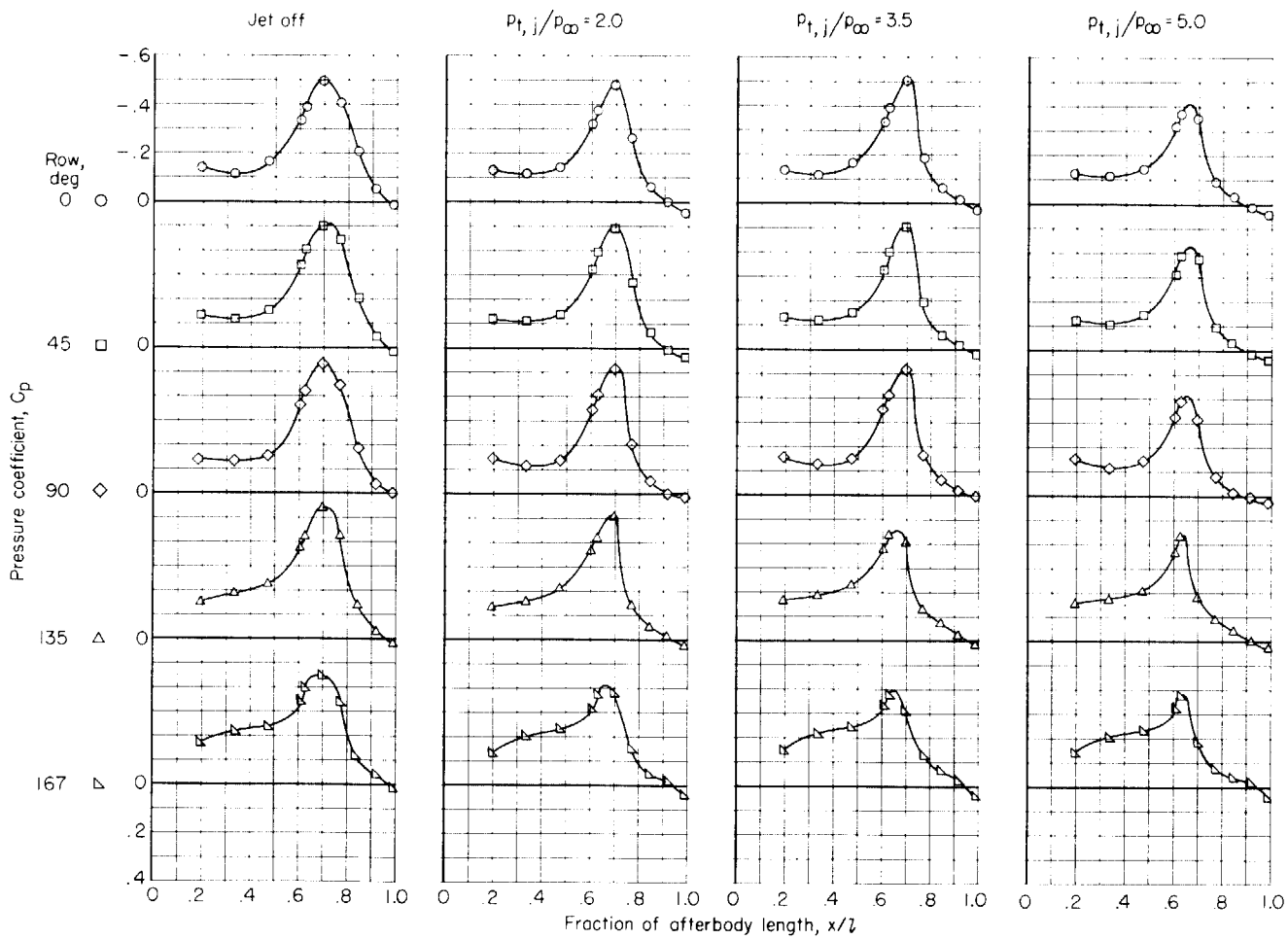

(d) M = 1.05.

Figure 14.- Concluded.

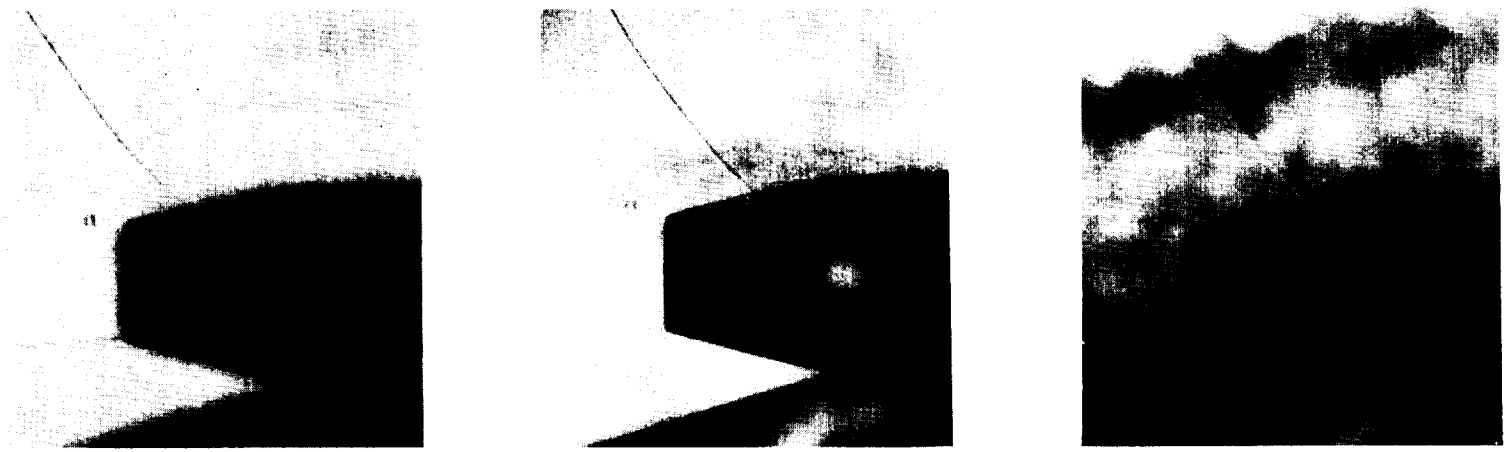

Jet off $\qquad$ $p_{t,j}/p_\infty = 2.0$ $\qquad$ $p_{t,j}/p_\infty = 5.0$

L-58-110a

Figure 15.- Shadowgraph illustrating movement of boattail shock on afterbody III with increasing jet total-pressure ratio. M = 1.00.

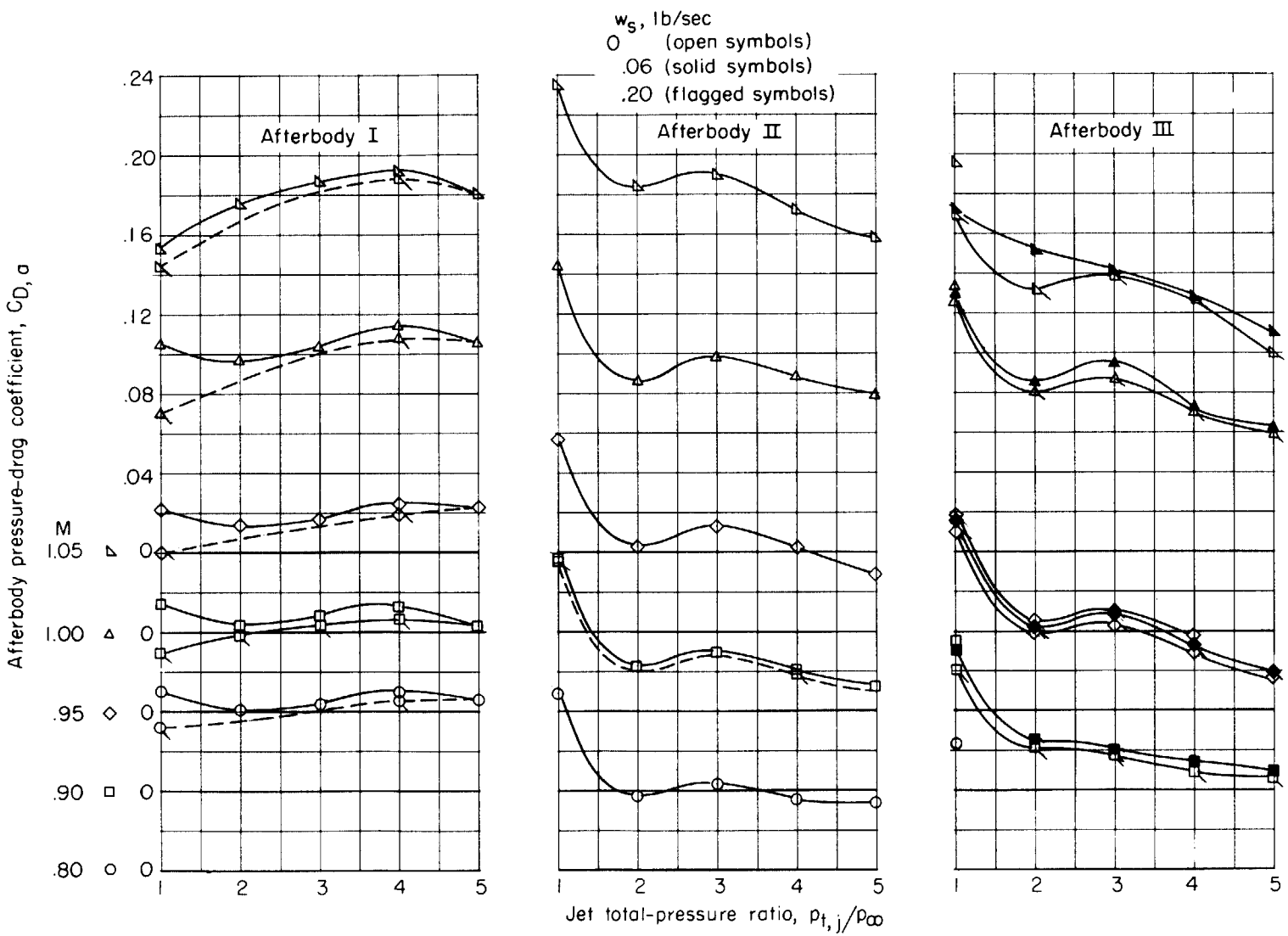

Figure 16.- Effect of jet total-pressure ratio on afterbody pressure-drag coefficients.

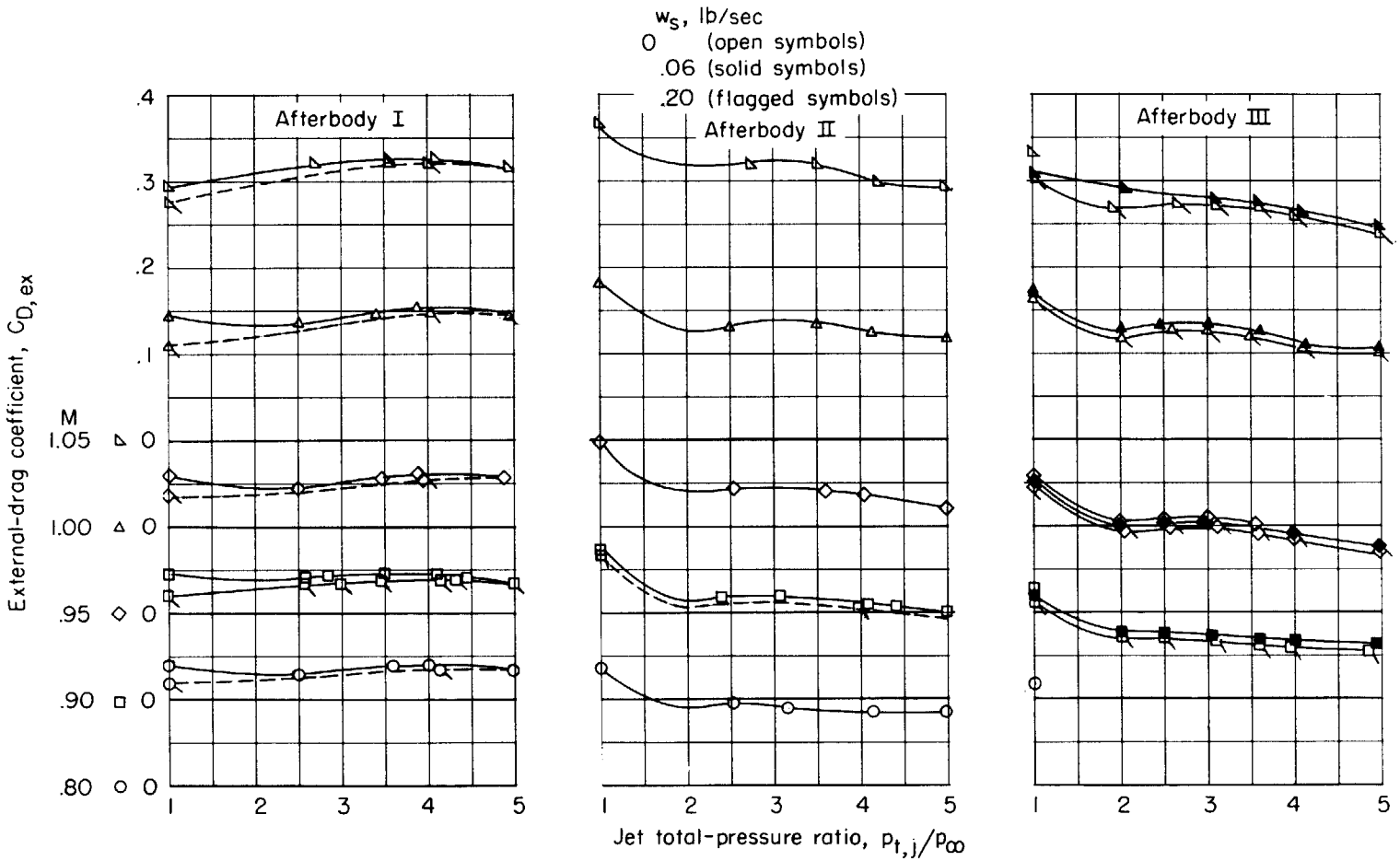

Figure 17.- Effect of jet total-pressure ratio on external-drag coefficients.

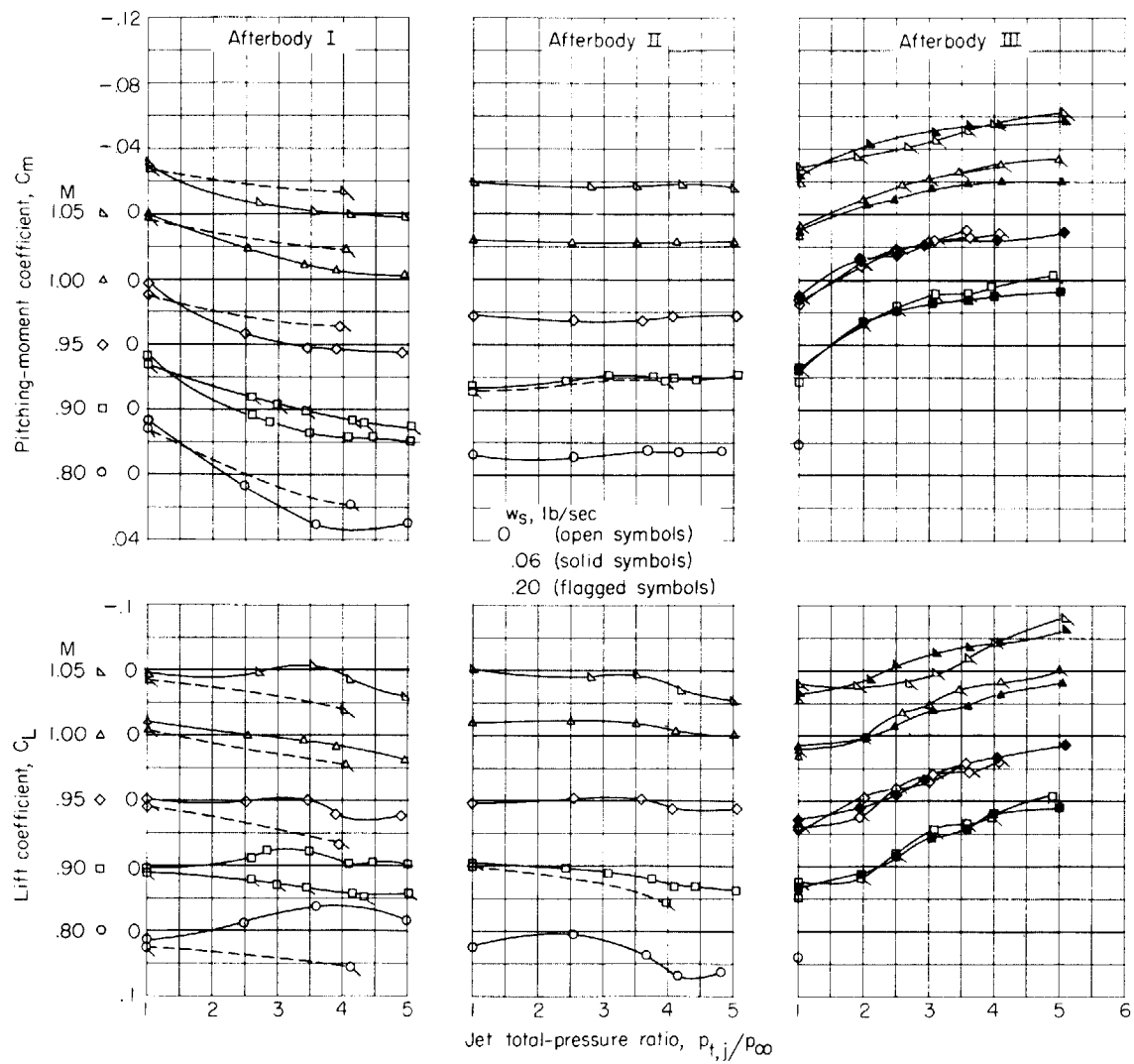

Figure 18.- Effect of jet total-pressure ratio on measured balance coefficients for pylon-supported nacelle model.

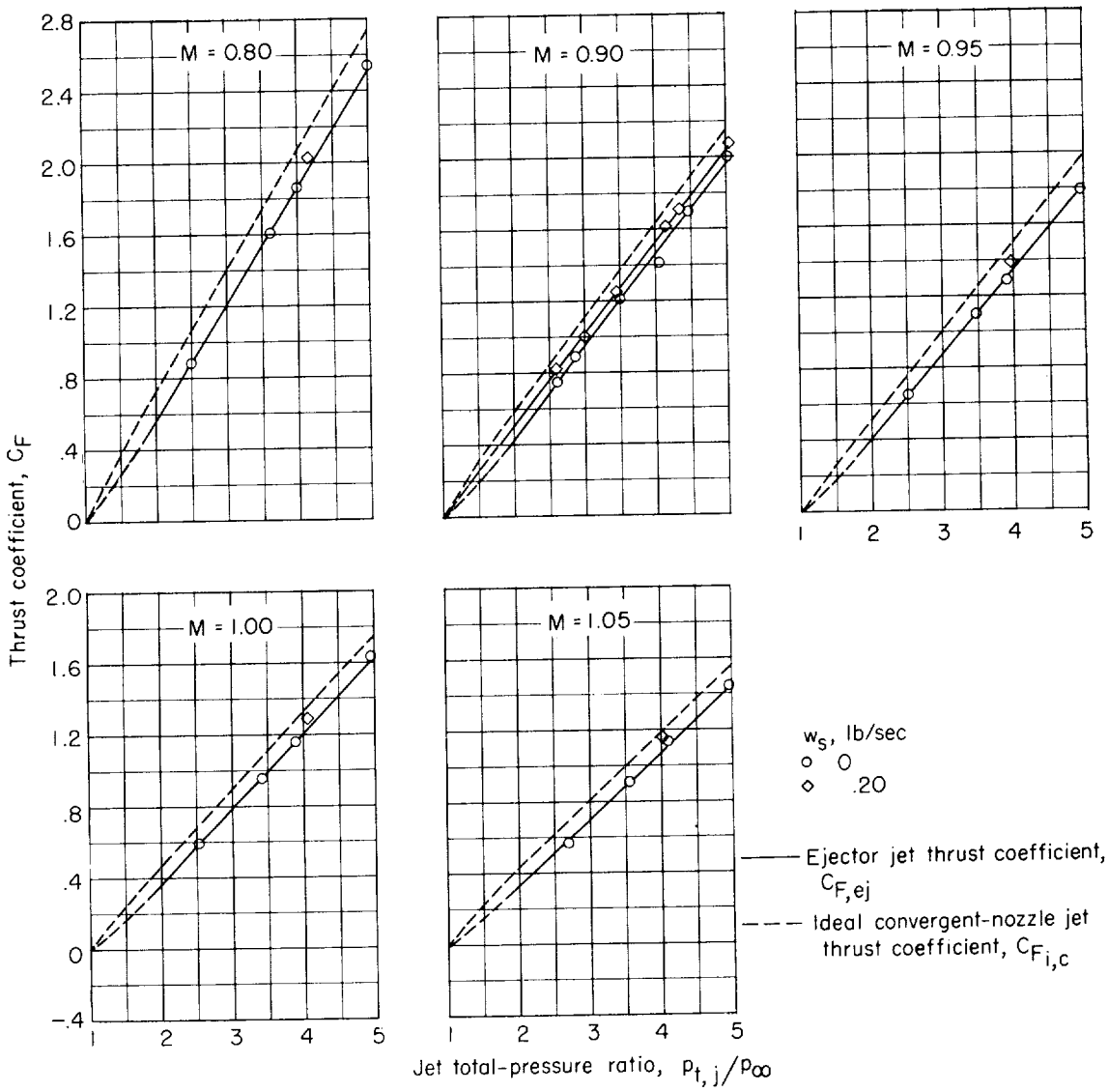

(a) Afterbody I.

Figure 19.- Variation of jet thrust coefficient with jet total-pressure ratio.

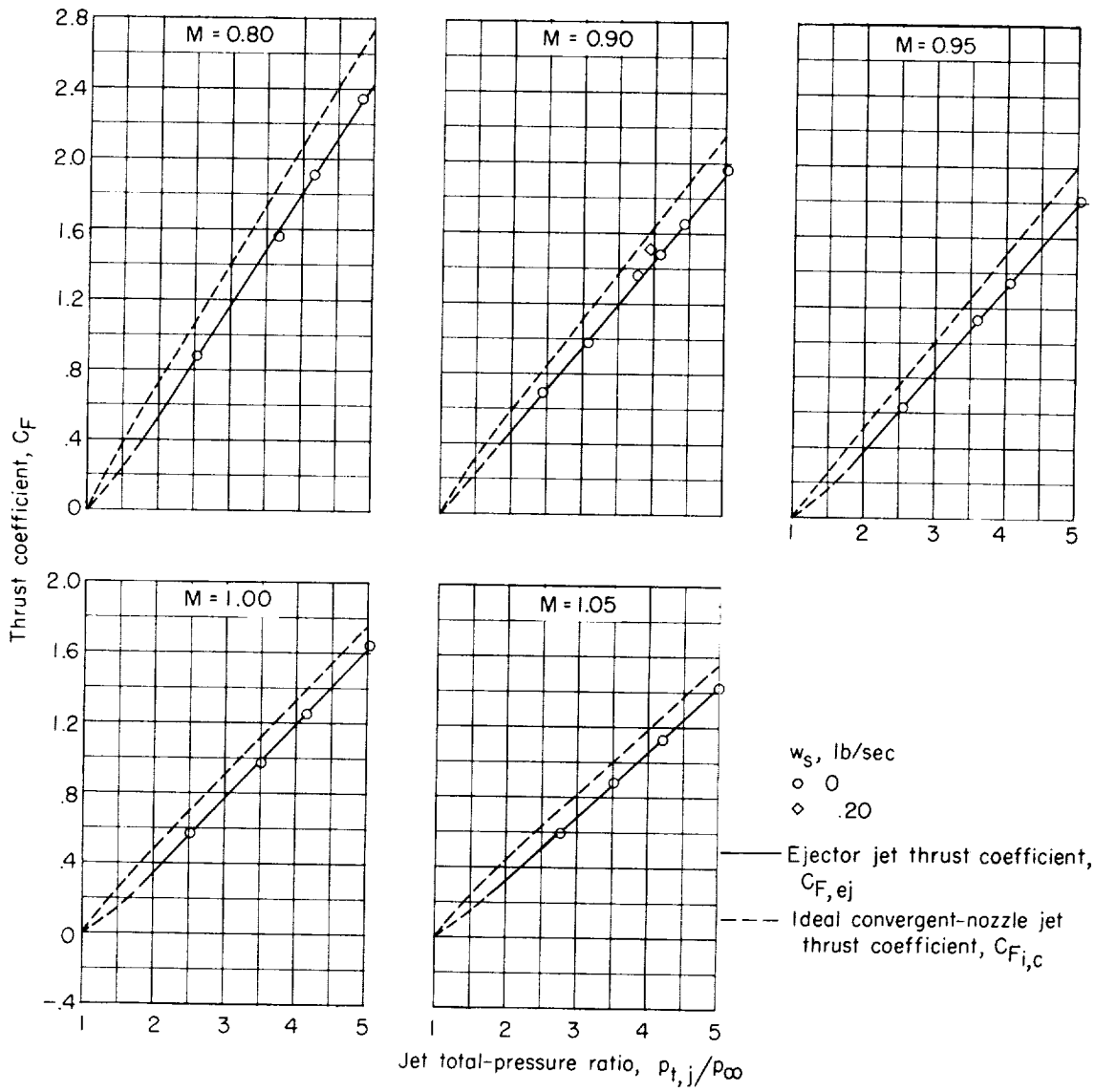

(b) Afterbody II.

Figure 19.- Continued.

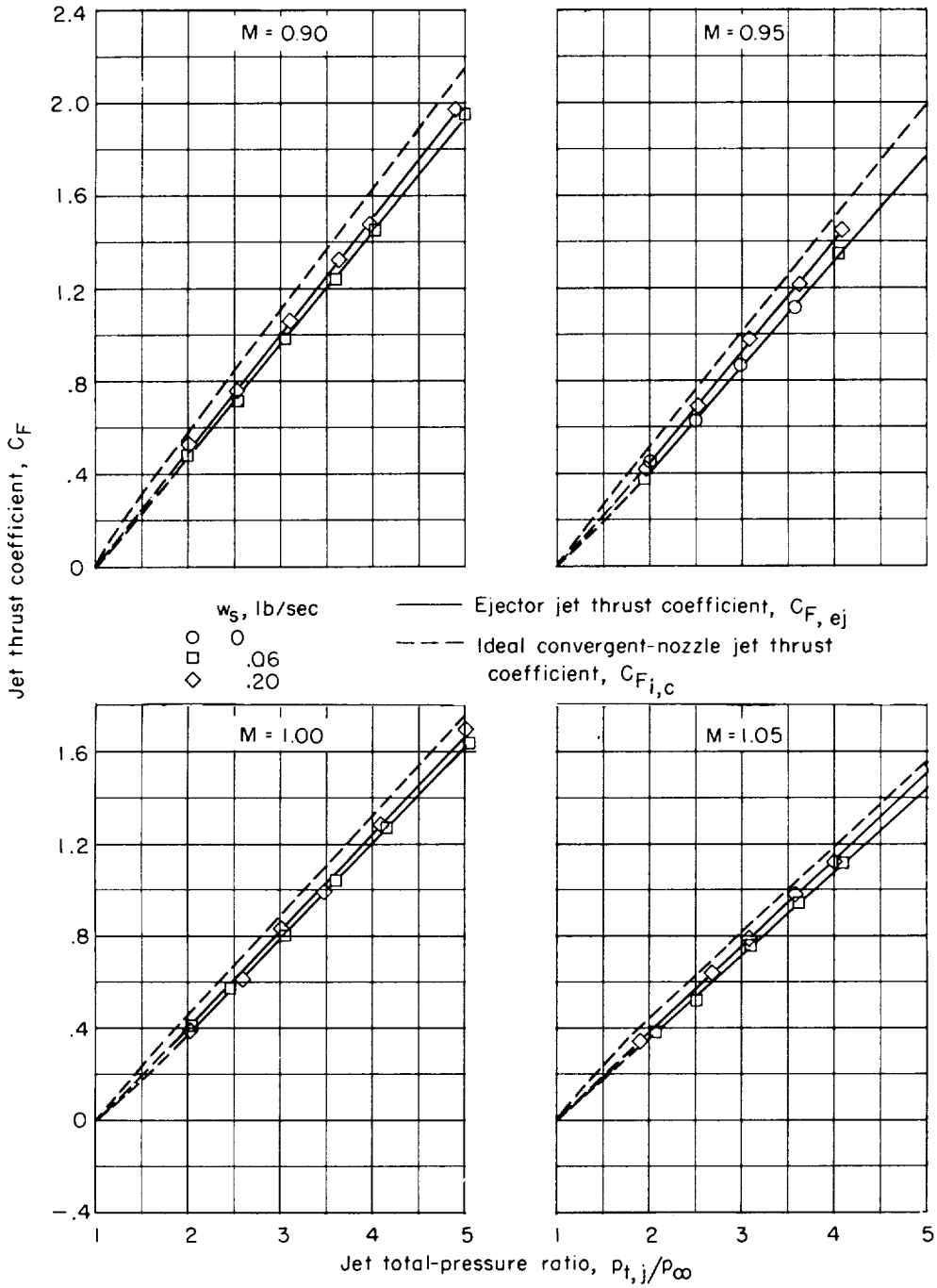

(c) Afterbody III.

Figure 19.- Concluded.

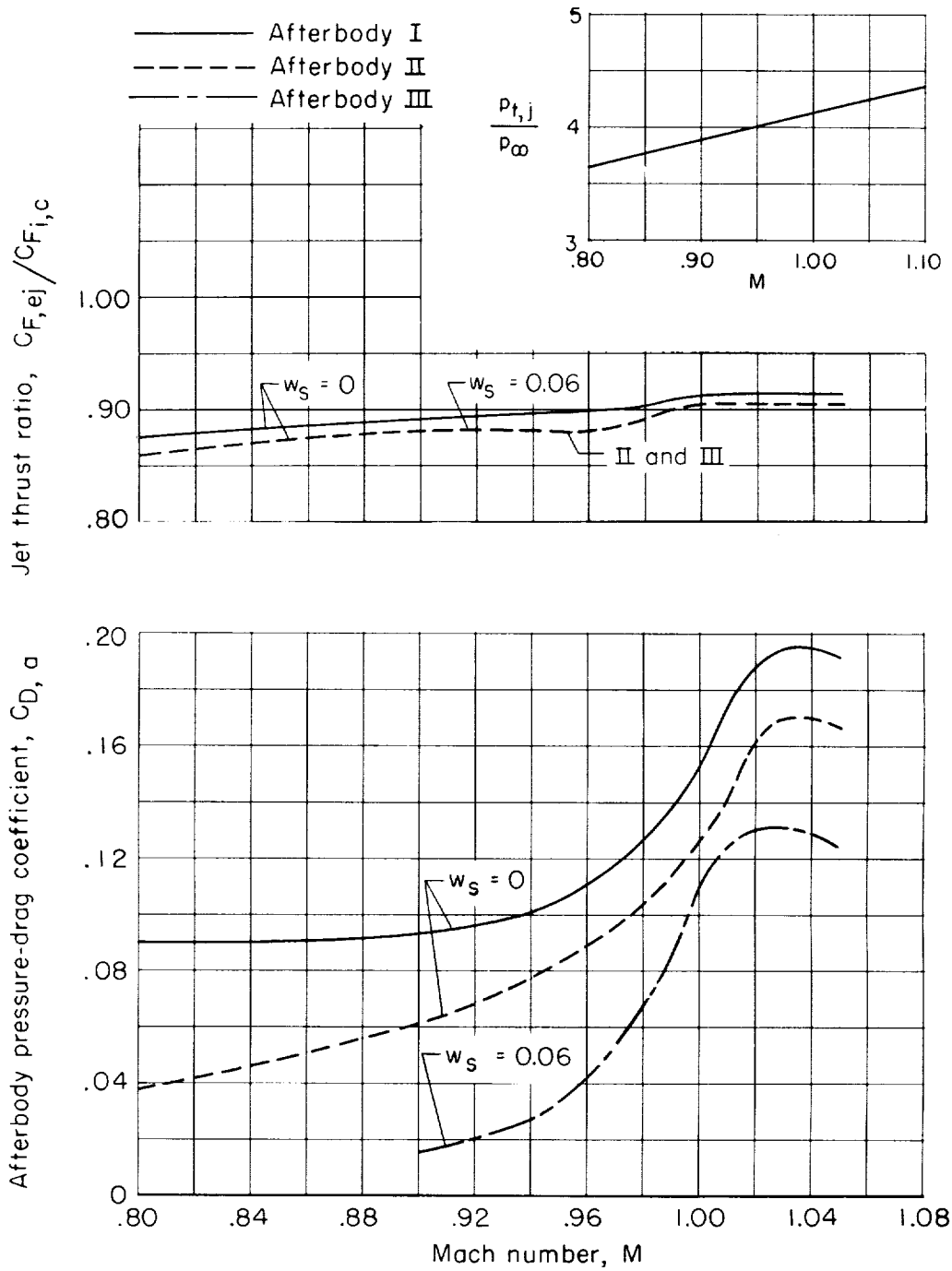

Figure 20.- Effect of Mach number on jet thrust ratio and afterbody pressure-drag coefficient. Data are presented for jet total-pressure ratios corresponding to the schedule with Mach number.

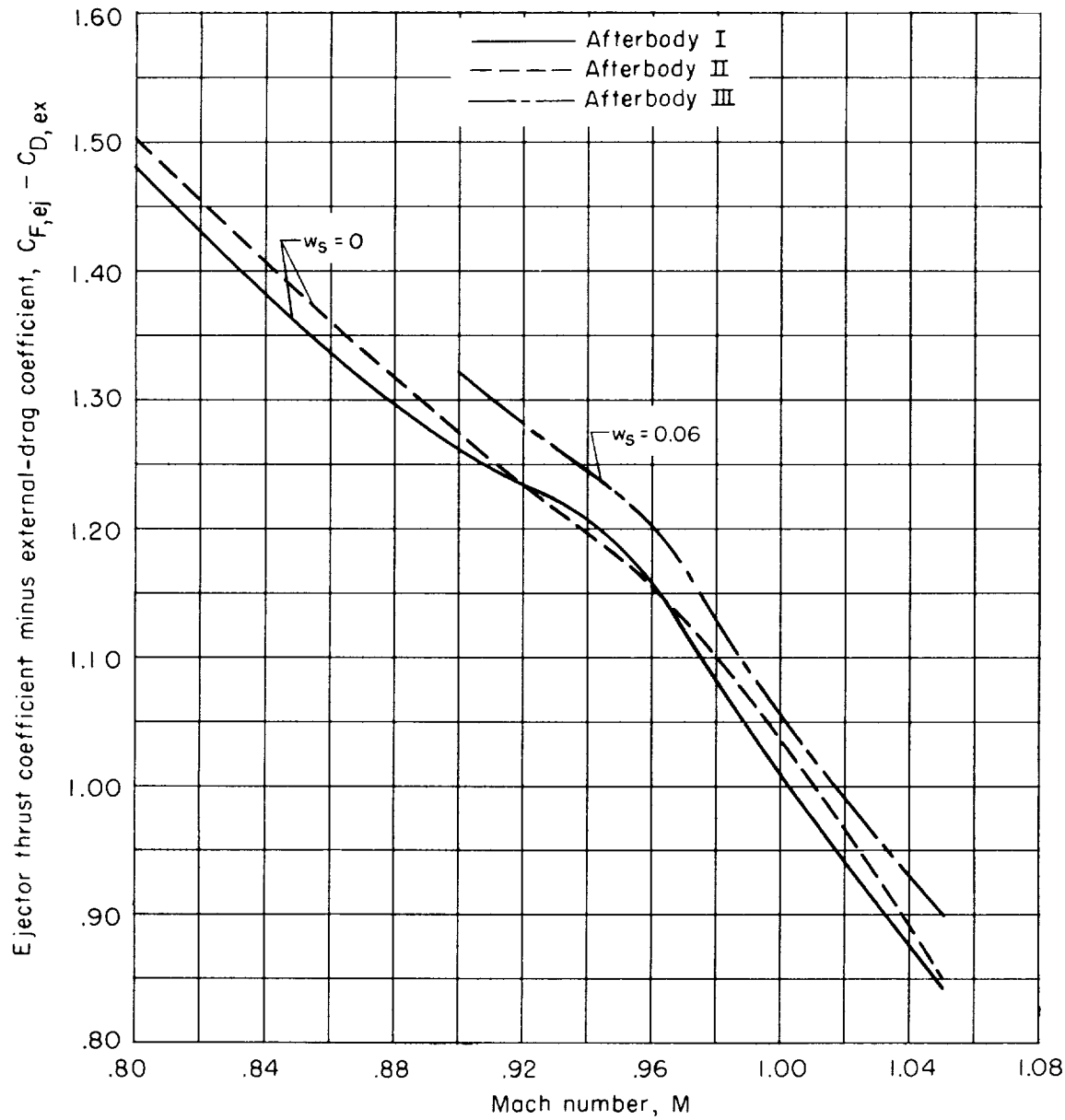

Figure 21.- Performance of the three afterbodies over the Mach number range. Data are presented for jet total-pressure ratios corresponding to the schedule with Mach number presented in figure 20.

NASA-Langley, 1962 L-133